

Article

Probing the Electronic Structure of Dinuclear Carbon-Rich Complexes Containing an Octa-3,5-diene-1,7-diyndiyl Bridging Ligand

Michael R. Hall , Stephen A. Moggach and Paul J. Low 

School of Molecular Sciences, University of Western Australia, 35 Stirling Highway, Crawley 6009, Australia

* Correspondence: paul.low@uwa.edu.au

Abstract: One electron oxidation of the monometallic alkenylacetylide complexes $[\text{Ru}\{\text{C}\equiv\text{CC}(\text{R})=\text{CH}_2\}(\text{dppe})\text{Cp}^*]$ (**1**) and $[\text{Ru}\{\text{C}\equiv\text{CC}(\text{R})=\text{CH}_2\}\text{Cl}(\text{dppe})_2]$ (**2**) ($\text{R} = \text{Ph}$ (**a**); $\text{R} = 4\text{-MeS-C}_6\text{H}_4$ (**b**)) generates in each case a dinuclear bis(allynylidene) complex $[\{\text{Ru}\}_2\{\mu\text{-C}=\text{C}=\text{C}(\text{R})\text{-CH}_2\text{-H}_2\text{C}-(\text{R})\text{C}=\text{C}=\text{C}\}][\text{PF}_6]_2$ ($\{\text{Ru}\} = \text{Ru}(\text{dppe})\text{Cp}^*$ (**[3a,b]**)[PF_6]₂); $\{\text{Ru}\} = \text{RuCl}(\text{dppe})_2$ (**[4a,b]**)[PF_6]₂), containing an unsaturated ethane bridge between both allynylidene moieties. Deprotonation of this ethane bridge results in the formation of the previously reported octa-3,5-diene-1,7-diyndiyl-bridged bimetallic species $[\{\text{Ru}\}_2\{\mu\text{-C}\equiv\text{CC}(\text{R})=\text{CH}\text{-HC}=(\text{R})\text{CC}\equiv\text{C}\}]\{\text{Ru}\} = \text{Ru}(\text{dppe})\text{Cp}^*$ (**5a,b**); $\{\text{Ru}\} = \text{RuCl}(\text{dppe})_2$ (**6a,b**). The isolation of these complexes illustrates a general synthetic route to these conjugated bimetallic species from monomeric alkenylacetylide precursors. Electrochemical and spectroelectrochemical investigations evince the ready formation of the representative redox series $[\mathbf{5a}]^{n+}$, and TD-DFT calculations performed on optimised structures featuring the simplified $\{\text{Ru}(\text{dmpe})\text{Cp}\}$ coordination sphere $[\{\text{Ru}(\text{dmpe})\text{Cp}\}_2\{\mu\text{-C}\equiv\text{CC}(\text{Ph})=\text{HC}\text{-CH}(\text{Ph})\text{CC}\equiv\text{C}\}]^{n+}$ ($[\mathbf{5a}^\dagger]^{n+}$) ($n = 0, 1, 2$) reveal significant delocalisation of the unpaired charge in the formally mixed-valent species ($n = 1$), consistent with Class III assignment within the Robin–Day classification scheme.



Citation: Hall, M.R.; Moggach, S.A.; Low, P.J. Probing the Electronic Structure of Dinuclear Carbon-Rich Complexes Containing an Octa-3,5-diene-1,7-diyndiyl Bridging Ligand. *Inorganics* **2024**, *12*, 20. <https://doi.org/10.3390/inorganics12010020>

Academic Editors: Francis Verpoort, Claudio Pettinari, Maurizio Peruzzini, Richard Layfield, Rainer Winter, Moris S. Eisen, Gábor Papp, Shuang Xiao and Axel Klein

Received: 14 November 2023

Revised: 14 December 2023

Accepted: 14 December 2023

Published: 1 January 2024



Copyright: © 2024 by the authors. Licensee MDPI, Basel, Switzerland. This article is an open access article distributed under the terms and conditions of the Creative Commons Attribution (CC BY) license (<https://creativecommons.org/licenses/by/4.0/>).

Keywords: organometallic complexes; cumulene; oxidative coupling; carbon-rich ligand; mixed-valence; Robin–Day classification

1. Introduction

Mixed-valent hetero- and homo-bimetallic complexes containing π -conjugated all-carbon and carbon-rich bridging ligands of the general form $[\{\text{L}_x\text{M}\}(\mu\text{-Bridge})\{\text{ML}_x\}]$ have drawn sustained interest as model systems with which to explore intramolecular electron and charge-transfer phenomena [1–3]. The orbital overlaps along the metal–bridge–metal assemblies are critical to the intramolecular electron transfer properties of the complex [4,5]; consequently, the chemical composition and structure of both the metal-ancillary ligand end-capping fragments, $\{\text{ML}_x\}$, and the bridging ligand afford a significant degree of control over these metal–bridge coupling interactions [6–8]. This electronic control by chemical design permits facile manipulation of the degree of (de)localisation along the molecular scaffold, facilitating the application of mixed-valent species as sensors, electrochromes or components for molecular electronics [9–13]. However, the relative orientation of the metal end-caps with respect to each other and features of low axial symmetry incorporated in the bridge can induce dynamic aspects in unconstrained systems that necessitate careful interpretation of data collected from measurements of the entire population with respect to any single conformation or structure [14–18].

Against this background, polyndiyl complexes of general form $[\{\text{L}_x\text{M}\}\{\mu\text{-C}\equiv\text{C}\}_n\{\text{ML}_x\}]$ can be identified as useful ‘all-carbon’ bridged systems and precursors through which to further explore chemical structure: electronic-property relationships and electron-transfer phenomena [19–24]. Within the metal capping fragments, $\{\text{ML}_x\}$, the energy and symmetry of the frontier metal d-orbitals can be manipulated through choice of the

metal [23,25–29] and ancillary ligands [30,31], which in turn mediates the extent of d-orbital overlap with the π -conjugated frontier orbitals of the polyynediyl bridge. Electrochemical measurements of polyynediyl complexes $[\{L_xM\}\{\mu-(C\equiv C)_n\}\{ML_x\}]$ typically reveal a decreasing separation of the first and second oxidation processes with increasing n , a phenomenon best attributed to the increasing spin delocalisation onto the carbon chain in the case of complexes of the heavier 4d and 5d metals [24,32,33], and increasingly localised metal-based redox processes for the lighter metal examples with more contracted and higher energy 3d fragment orbitals [8,20,27].

As a consequence of the increasing carbon character in the frontier orbitals of the heavier metal complexes, spectroscopic studies of the redox products derived from these all-carbon-bridged species $[\{L_xM\}\{\mu-(C\equiv C)_n\}\{ML_x\}]$ are generally limited to the $n = 1, 2$ and 3 examples, the latter being only possible in the case of complexes bearing sterically demanding ancillary ligands [8]. This recalls the use of large end-groups to stabilise very long polyynes employed by, for example, Walton [34,35] and Tykwinski [36]. For smaller ancillary ligand sets, dimerisation of the radicals derived from the hexatriynediyl-bridged complexes has been reported from spectroelectrochemical (SEC) and preparative scale chemical oxidation of these complexes, hindering further experimental measurements [37].

Metal polyendiyl complexes $[\{L_xM\}\{\mu-(CH=CH)_n\}\{ML_x\}]$ are also known [38,39], and although spectroscopic studies of the redox products derived from these complexes are rare [40], a number of electrochemical studies have hinted at the efficacy of charge transport through the polyene chain [41–43]. The bridging structures themselves are intriguing as the functionalisation these sp^2 centres, a feature not possible with polyynediyl ligands composed of sp carbon centres, which would allow introduction of electron-donating or -withdrawing groups to stabilise charges along the carbon-rich backbone [44].

In seeking to develop longer bridging ligands with increased chemical stability in the mixed-valent state, attention has been largely drawn to ‘carbon-rich’ derivatives of these metal-alkynyl structures. As a result, there are numerous examples of bimetallic complexes and mixed-valence systems derived from bridging ligands featuring metal-alkynyl and -vinyl fragments and a host of interpolated arylene fragments [1,20,45,46]. The studies of such compounds, augmented by advances in (TD-)DFT methods, have been critical to unravelling further details of the electronic structure and nature of mixed-valence compounds and complexes [5,47–51] and also the fundamentals of the electron transfer reaction in both the ground and excited states [52–54]. However, whilst these compounds have allowed significant advances to be made in both the synthesis and subsequent analysis of these mixed-valent derivatives bridged by all-carbon or carbon-rich ligands, the inclusion of aromatic spacing groups introduces a degree of conformational uncertainty and significantly alters the underlying electronic structures [15–17,55,56].

Resting between these structure types are less well-explored families of complexes featuring hybrid bridging ligands containing both alkynyl/ethynyl and vinyl/enyl motifs [57–62]. We have recently reported the synthesis of a range of bimetallic ruthenium complexes containing an octa-3,5-diene-1,7-diyl bridging ligand $[\{Ru(dppe)Cp^*\}_2\{\mu-C\equiv CC(R)=CH-HC=(R)C\equiv CC\}]$ (**5**), formed via in situ oxidation of $[Ru\{C\equiv CC(R)=CH_2\}(dppe)Cp^*]$ [63] and sequential dimerisation and deprotonation [64]. Containing a highly conjugated carbon-rich bridging ligand, readily modified by aryl side groups, R, complexes **5** present as a structural motif, complementary to the polyynediyl, polyendiyl, diethynylarylene or divinylarylene complexes discussed above, through which to study electronic structure and electron-transfer processes in mixed-valence complexes (Figure 1).

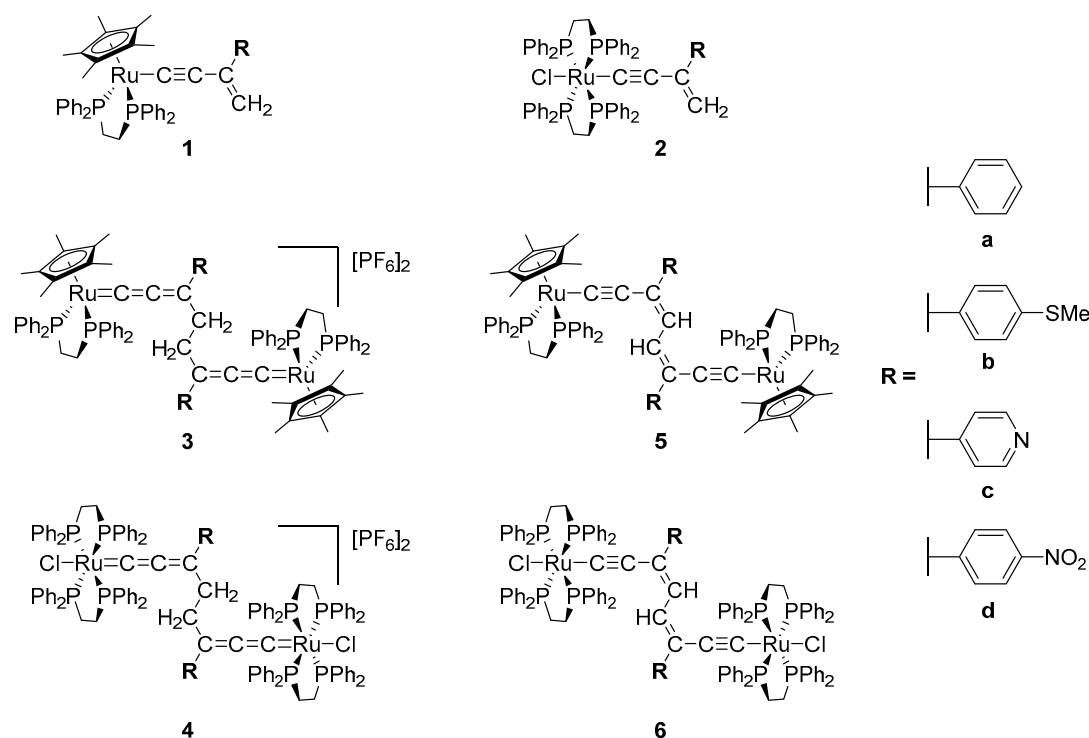
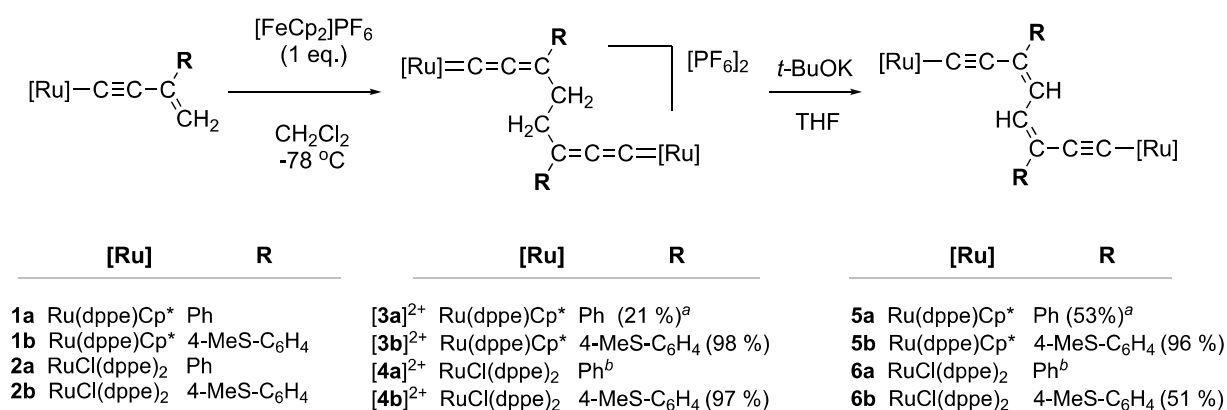


Figure 1. Compounds discussed in this study.

Here, we report further investigation of the electronic properties of these coupled products, alongside a modified stoichiometric oxidative coupling procedure that provides a more rational synthesis of these compounds (Scheme 1). For the series $[\{\text{Ru}(\text{dppe})\text{Cp}^*\}_2\{\mu\text{-C}\equiv\text{CC}(\text{R})=\text{HC}-\text{CH}(\text{R})\text{CC}\equiv\text{C}\}]$, UV-Vis-NIR measurements supported by TD-DFT calculations performed on the model complexes $[\{\text{Ru}(\text{dmpe})\text{Cp}\}_2(\mu\text{-C}\equiv\text{CC}(\text{Ph})=\text{HC}-\text{CH}(\text{Ph})\text{CC}\equiv\text{C})]^{n+}$ ($[\text{5a}^+]^{n+}$, $n = 0, 1, 2$), with analysis of the natural transition orbitals (NTOs) of the associated transitions, allow formal assignment of $[\text{5}]^+$ as a strongly delocalised, Robin and Day Class III, mixed-valent species.



Scheme 1. Formation of ethane-bridged dinuclear bis(alkenylidene) complexes $[\text{3,4}]^{2+}$ and subsequent octa-3,5-diene-1,7-diyndiyl-bridged bimetallic species **5,6**. ^a Previously reported [64]. ^b Generated as a component of a crude product mixture that could not be purified.

2. Results and Discussion

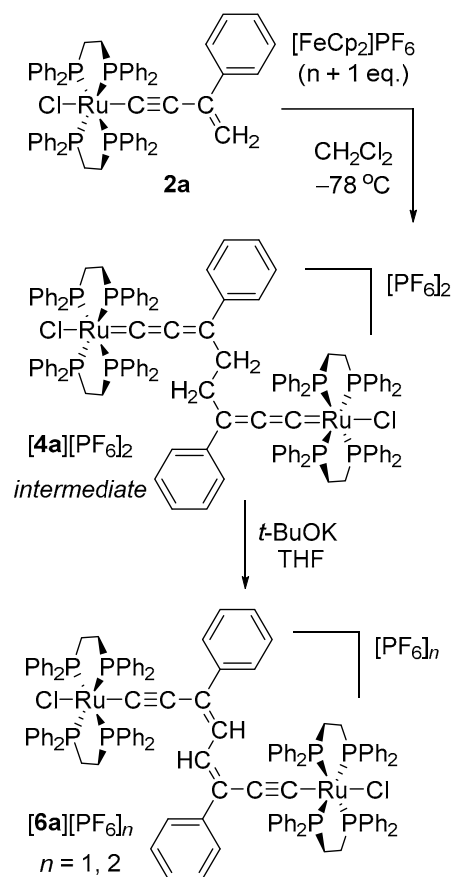
2.1. Synthesis

Solutions of alkenylacetylide complexes $[\text{Ru}\{\text{C}\equiv\text{CC}(\text{R})=\text{CH}_2\}(\text{dppe})\text{Cp}^*]$ are known to readily dimerise following aerial oxidation, resulting in the initial formation of ethane-bridged

bis(allynylidene) complexes $[\text{Ru}(\text{dppe})\text{Cp}^*]_2\{\text{C}=\text{C}=\text{C}(\text{R})-\text{CH}_2-\text{H}_2\text{C}(\text{R})-\text{C}=\text{C}=\text{C}\}[\text{PF}_6]_2$ [3][PF₆]₂. In turn, complexes [3][PF₆]₂ readily deprotonate to give bimetallic complexes $[\{\text{Ru}(\text{dppe})\text{Cp}^*\}_2\{\text{C}\equiv\text{CC}(\text{R})=\text{HC}-\text{CH}=\text{C}(\text{R})\text{C}\equiv\text{C}\}]$ (5) containing octa-3,5-diene-1,7-diyl bridging ligands (Scheme 1) [64]. In an effort to expand the scope of this reaction, the alkenylacetylide complexes $[\text{Ru}\{\text{C}\equiv\text{CC}(\text{R})=\text{CH}_2\}(\text{dppe})\text{Cp}^*]$ (1a, R = Ph; 1b, R = C₆H₄Me-4) and $[\text{Ru}\{\text{C}\equiv\text{CC}(\text{R})=\text{CH}_2\}\text{Cl}(\text{dppe})_2]$ (2a, R = Ph; 2b, R = C₆H₄Me-4) were each treated with one equivalent of [FeCp]₂PF₆ to promote 1-electron oxidation (noting the relatively low first oxidation potential of 1a (−0.14 V vs. ferrocene/ferrocenium)) [64] and allowed to stir in solution for 2 h to promote dimerisation. Work-up afforded the ethane-bridged bis(allynylidene) complexes [3a,b][PF₆]₂ and [4a,b][PF₆]₂ (Scheme 1), characterised by the intense $\nu(\text{C}=\text{C}=\text{C})$ bands near 1920 cm^{−1}, as well as resonances in the ¹H NMR spectrum near δ 1.9 ppm arising from the protons of the ethane bridge. Deprotonation of [3a,b][PF₆]₂ and [4a,b][PF₆]₂ by treatment with *t*-BuOK in THF gave the bis(acetylide) complexes 5a,b and 6a,b (Scheme 1) characterised by $\nu(\text{C}\equiv\text{C})$ bands near 2030 cm^{−1}, with other spectroscopic characteristics in agreement with those previously reported for similar compounds [64]. Related chemistry from ethane-bridged bis(carbyne) complexes leading to bis(vinylidene) and ultimately butadienydiyl complexes on rhenium scaffolds is also noted as providing precedence for such transformations of carbon-rich scaffolds [65].

The bimetallic complexes [4][PF₆]₂ and 6 featuring the {RuCl(dppe)₂} coordination sphere were poorly soluble in most common solvents, limiting the extent to which they could be characterised, especially via ¹³C{¹H} NMR spectroscopy. This limited solubility also hampered efforts at obtaining pure samples, and as such [4a][PF₆]₂ could only be obtained as part of a crude mixture. Furthermore, attempts to deprotonate this complex within this mixture gave a solid from which spectroscopic evidence supported the formation of 6a, but which could not be satisfactorily purified. However, oxidation of 2a with two or three equivalents [FeCp]₂PF₆, followed by treatment of the reactions solution with *t*-BuOK, permitted isolation of the more soluble and hence more readily purified monocationic and dicationic complexes [6a]PF₆ (30% isolated yield) and [6a][PF₆]₂ (19% isolated yield), respectively (Scheme 2). In this modified one-pot, two-step procedure, any amount of [4a]²⁺ formed from the initial oxidation of 2a is deprotonated in situ upon the addition of a base to give 6a (as part of a complex mixture), which is then further oxidised with the remaining equivalent(s) of ferrocenium.

Single crystals of [6a]PF₆ were grown from the slow diffusion of MeOH into a CH₂Cl₂ solution of the complex and these were characterised by X-ray diffraction (Figure 2, Table 1). An inversion centre in the mid-point of the central C4–C4A bond renders each half of the cation identical, necessitating caution in any discussion of mixed-valence characteristics based on the structural data. Nevertheless, the Ru1–C1 [1.958(4) Å], C1–C2 [1.217(6) Å], C2–C3 [1.400(6) Å] and C3–C4 [1.401(6) Å] bond lengths show modestly reduced bond length alternation compared with the bridging ligands in complexes 5 [64], consistent with involvement of the bridging ligand in the redox process [66]. These observations are also consistent with the conclusions drawn from electrochemical and spectroelectrochemical studies of 5a, and related species, which undergo two sequential one-electron oxidations to give the delocalised ‘mixed-valent’ complex [5a]PF₆ and the crystallographically characterised bis(allynylidene) [5a][PF₆]₂ [64].



Scheme 2. A schematic showing the synthesis of $[\mathbf{6a}][\text{PF}_6]_n$ ($n = 1, 2$) via $[\mathbf{4a}][\text{PF}_6]_2$; note that the additional equivalents of $[\text{FeCp}_2]\text{PF}_6$ added at the commencement of the reaction drive the oxidation of $\mathbf{6a}$ to $[\mathbf{6a}][\text{PF}_6]_n$ ($n = 1, 2$).

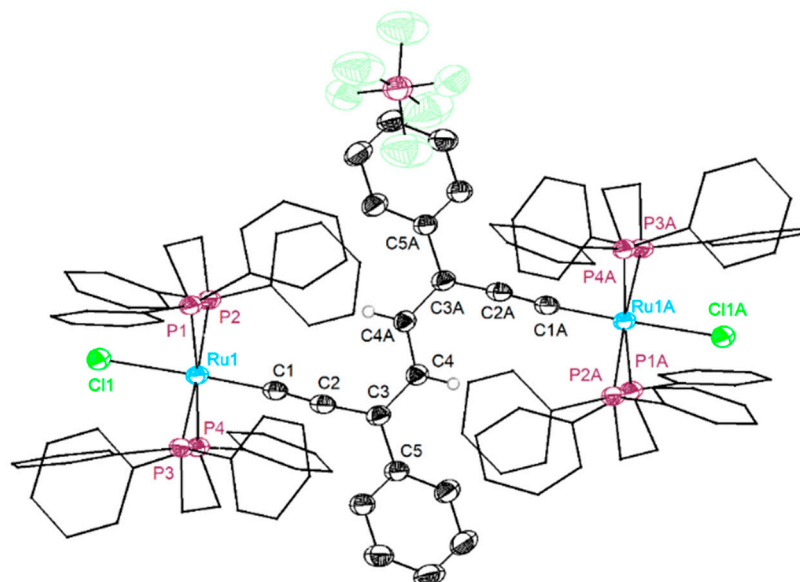
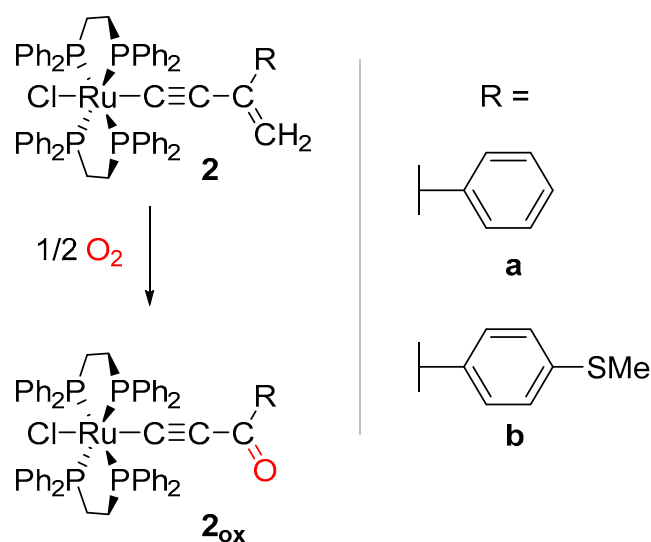


Figure 2. Molecular structure of $[\mathbf{6a}]\text{PF}_6$ showing the atom labelling scheme. Selected hydrogen atoms are omitted and dppe ligands drawn in wireframe for clarity. Thermal ellipsoids are shown at the 50% level.

Table 1. Selected bond lengths (Å) and angles (°) from the crystallographically determined structure of [6a]PF₆.

[6a]PF ₆	
Ru1-P1	2.3729 (11)
Ru1-P2	2.3946 (11)
Ru1-P3	2.3803 (11)
Ru1-P4	2.3934 (11)
Ru1-Cl1	2.4591 (11)
Ru1-C1	1.958 (4)
C1-C2	1.217 (6)
C2-C3	1.400 (6)
C3-C4	1.401 (6)
C4-C4A	1.403 (9)
C3-C5	1.490 (6)
Ru1-C1-C2	175.1 (4)
C1-C2-C3	175.4 (4)
C2-C3-C4	121.1 (4)
C3-C4-C4A	124.3 (5)
C4-C3-C5	119.4 (4)

Beyond these solution-based chemical oxidation reactions, aerial oxidation of the alkene unit occurred over the course of several weeks when solid samples of **2a** and **2b** were stored under ambient conditions, resulting in the formation of the alkynylketone complexes **2a_{ox}** and **2b_{ox}** in a manner similar to that observed previously for related samples (Scheme 3) [63,67]. Both **2a_{ox}** and **2b_{ox}** were structurally characterised by single crystal X-ray diffraction (Figure 3, Table 2) in addition to the conventional spectroscopic methods. These carbonyl species were differentiated from their alkenylacetylide precursors by a characteristically low-energy shift of the $\nu(\text{C}\equiv\text{C})$ band at ca. 2000 cm^{-1} , reflecting the conjugation of the alkynyl and carbonyl moieties, the absence of geminal proton signals in the ¹H NMR spectra, as well as observation of the appropriate cationic ion envelope by ESI(+)-MS. The formation of these complexes necessitated the storage of solid samples of **1** and **2** under an inert atmosphere.

**Scheme 3.** Alkynylketone complexes **2a_{ox}** and **2b_{ox}** generated from aerial oxidation of alkenylacetylide complexes **2a** and **2b**.

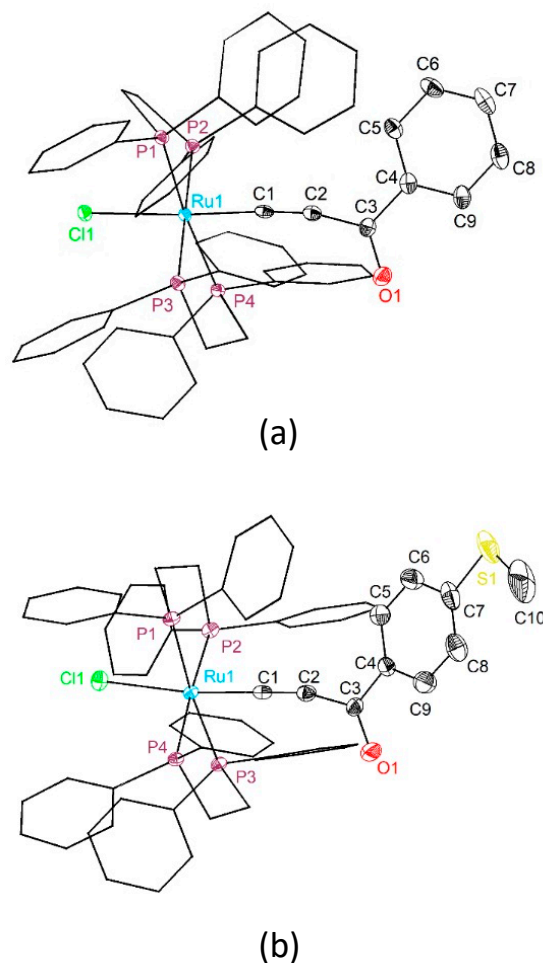


Figure 3. Molecular structures of (a) **2a_{ox}** and (b) **2b_{ox}** (right) showing the atom labelling scheme. Hydrogen atoms are omitted and dppe ligands drawn in wireframe for clarity. Thermal ellipsoids are shown at the 50% level.

Table 2. Selected bond lengths (Å) and angles (°) from the crystallographically determined structures of **2a_{ox}** and **2b_{ox}**.

	2a_{ox}	2b_{ox}
Ru1-P1	2.3884(5)	2.3944(15)
Ru1-P2	2.3979(5)	2.3529(14)
Ru1-P3	2.3407(5)	2.3860(15)
Ru1-P4	2.3612(5)	2.3856(15)
Ru1-Cl1	2.5067(5)	2.5053(15)
Ru1-C1	1.986(2)	1.972(6)
C1-C2	1.196(3)	1.218(9)
C2-C3	1.428(3)	1.424(9)
C3-C4	1.495(3)	1.497(9)
O1-C3	1.245(3)	1.240(8)
Ru1-C1-C2	175.58(17)	178.2(5)
C1-C2-C3	167.6(2)	166.0(7)
C2-C3-C4	119.45(18)	119.3(6)

2.2. Electronic Structure Calculations and Spectroscopy

To better rationalise the course of the reactions leading from complexes **1** and **2** to **5** and **6**, and the sequence of redox reactions that characterise the bimetallic compounds, (TD-)DFT calculations (BLYP35/COSMO(CH₂Cl₂)/Ru(LANL2DZ)/all other atoms 6-31G**) were

performed on the representative model structures $[\text{Ru}\{\text{C}\equiv\text{C}(\text{Ph})=\text{CH}_2\}(\text{dmpe})\text{Cp}]$ (1a^\dagger) and $[\{\text{Ru}(\text{dmpe})\text{Cp}\}_2(\mu\text{-C}\equiv\text{C}(\text{Ph})=\text{HC}-\text{CH}(\text{Ph})\text{CC}\equiv\text{C})]$ (5a^\dagger), featuring the simplified $\{\text{Ru}(\text{dmpe})\text{Cp}\}$ coordination sphere (Figure 4), and their oxidation products $[1\text{a}^\dagger]^+$ and $[5\text{a}^\dagger]^{n+}$ ($n = 1, 2$) (dmpe = bis(dimethylphosphino)ethane). As has been demonstrated by Kaupp and others elsewhere [49,68], the BLYP35 global hybrid functional, used in concert with a COSMO solvent model, provides a balance between accuracy and computational efficiency in accurately describing localised vs. delocalised mixed-valence complexes. The optimised geometries determined in this manner, and which were verified as true minima through the absence of imaginary frequencies, are in good agreement with the formal valence bond descriptions of these species.

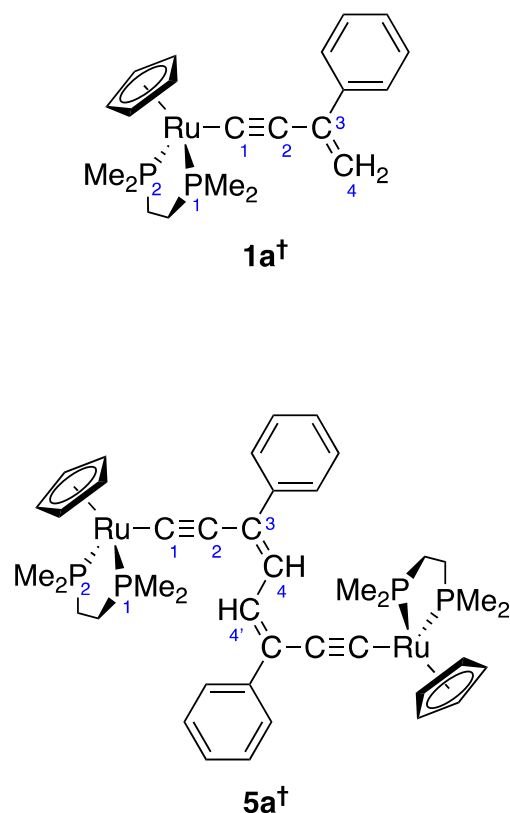


Figure 4. The computational model compounds 1a^\dagger and 5a^\dagger , and the associated atom labelling scheme.

The use of simplified ancillary ligand sets in model calculations of this type has been shown to provide results in good agreement with larger models and experiment [69]. Here, the close agreement of the calculated $\nu(\text{C}\equiv\text{C})$ frequencies (after application of a scaling factor 0.93) [70] for 1a^\dagger (2043 cm^{-1}) and 5a^\dagger (2024 cm^{-1}) with those observed for 1a (2057 cm^{-1}) [63] and 5a (2036 cm^{-1}) [64] gives further confidence in the validity of these models.

The HOMO of 1a^\dagger has appreciable contribution from the buta-3-ene-ynyl ligand (46%), which includes significant $\text{C}_\delta\text{H}_2$ character (15%). This observation helps rationalise the heightened nucleophilicity and propensity for this site to enter into reactions with electrophiles (Figure 5a) [63]. The removal of one electron from 1a^\dagger affords the radical cation $[1\text{a}^\dagger]^+$, with analysis of the frontier orbital composition revealing that both the α - and β -HOSO have significant character at $\text{C}_\delta\text{H}_2$ (25 and 14% respectively), providing a rationale for the selective $\text{C}_\delta\text{-C}_\delta$ coupling observed following oxidation of **1**, and, by analogy, **2** (Figure 5a).

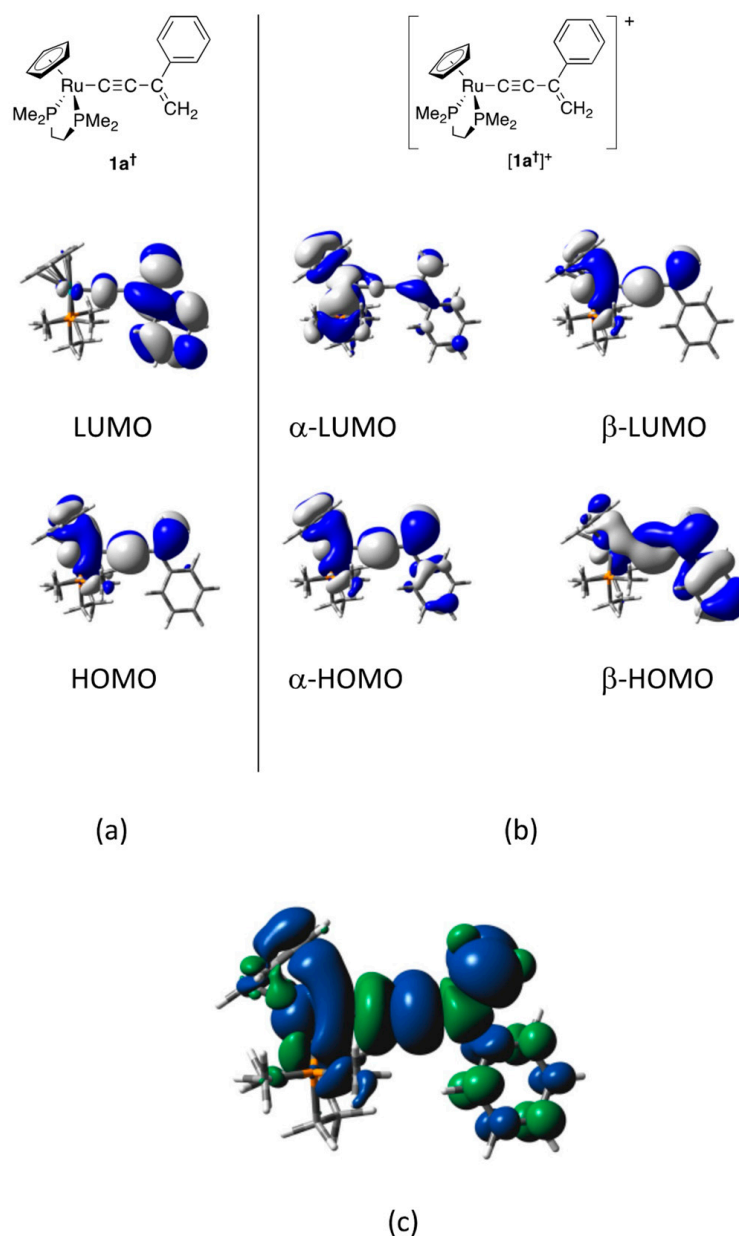
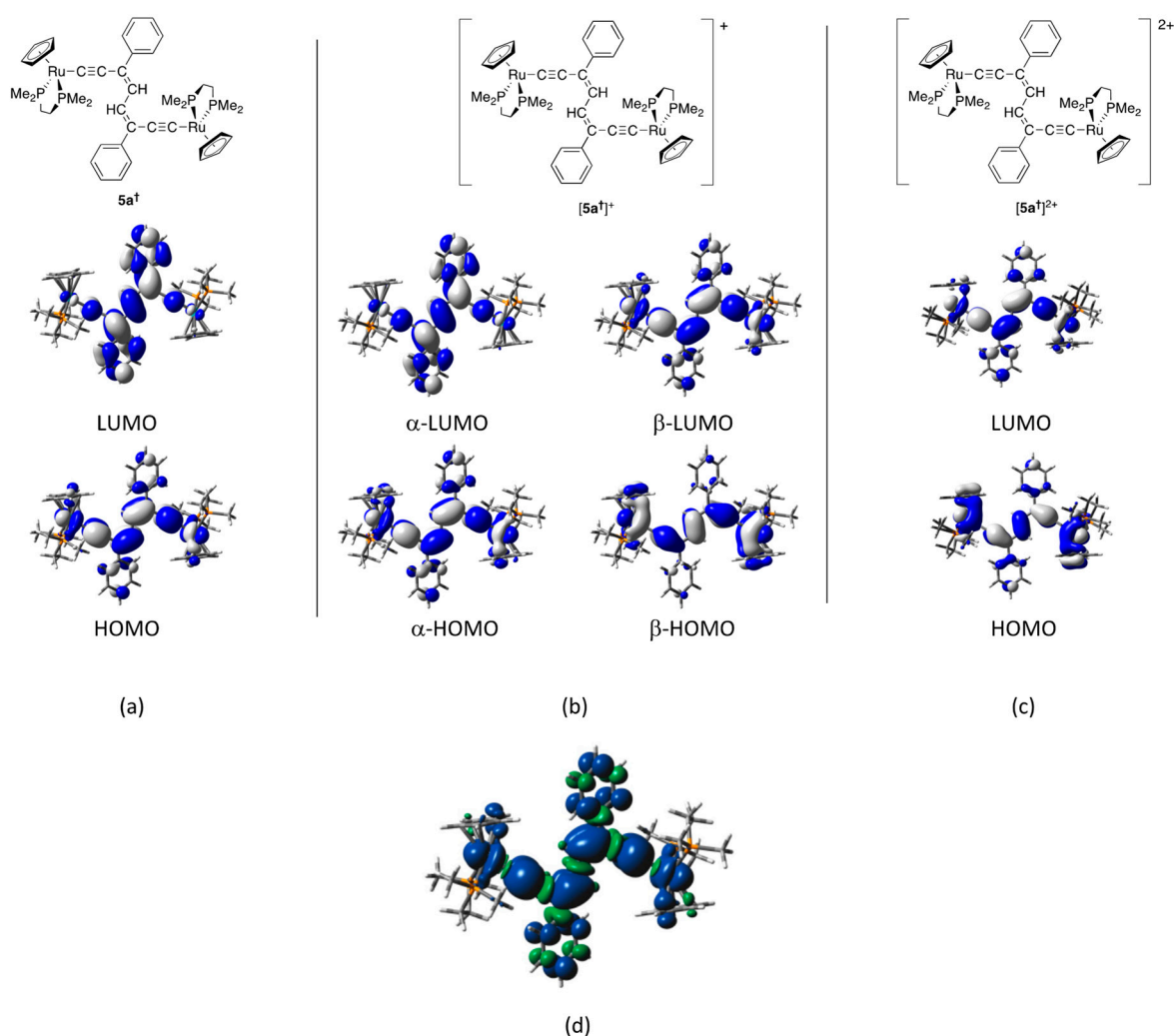


Figure 5. Plots (contours at $\pm 0.02 (e/\text{bohr}^3)^{1/2}$) of the frontier molecular (spin) orbitals of $[1a^\dagger]^{n+}$ ((a) $n=0$; (b) $n=1$), and spin density plot of $[1a^\dagger]^+$ (c).

Turning to the bimetallic model $5a^\dagger$, the bond lengths and angles in the DFT-optimised geometry (Table 3) and the nodal pattern of the HOMO (Figure 6) are consistent with the description of the carbon-rich bridging ligand as an octa-3,5-diene-1,7-diyndiyl fragment (Scheme 1). The 10-atom RuC_8Ru ($\text{Ru}-\text{C}\equiv\text{C}-\text{C}(\text{Ph})=\text{CH}-\text{CH}=\text{C}(\text{Ph})-\text{C}\equiv\text{C}-\text{Ru}$) chain features heavily in the frontier orbitals with a significant contribution from the carbon atoms of the diene-diyndiyl bridge (HOMO, $\text{Ru}/\text{C}_{10}/\text{Ru}$ 10/63/10%; LUMO, $\text{Ru}/\text{C}_{10}/\text{Ru}$ 2/58/2%), which is reminiscent of the frontier orbital composition of polyyndiyl $[\{\text{Cp}^*(\text{dppe})\text{Ru}\}\{\mu-(\text{C}\equiv\text{C})_n\}\{\text{Ru}(\text{dppe})\text{Cp}^*\}]$ complexes [14,27,71–73].

Table 3. Selected bond lengths (Å) and angles (°) from the optimised structures of $[1a^{\dagger}]^{n+}$ ($n = 0, 1$) and $[5a^{\dagger}]^{n+}$ ($n = 1, 2$) (labelling as per Figure 4).

	$1a^{\dagger}$	$[1a^{\dagger}]^+$	$5a^{\dagger}$	$[5a^{\dagger}]^+$	$[5a^{\dagger}]^{2+}$
Ru1-P1	2.3137	2.3572	2.3226/2.3136	2.3260/2.3253	2.3446/2.3434
Ru1-P2	2.3084	2.3393	2.3071/2.3075	2.3166/2.3176	2.3292/2.3287
Ru1-C1	2.0293	1.9633	2.0278/2.0286	1.9661/1.9687	1.9114/1.9117
C1-C2	1.2283	1.2372	1.2301/2.0286	1.2437/1.2433	1.2591/1.2587
C2-C3	1.4307	1.4195	1.4250/1.4251	1.3884/1.3891	1.3565/1.3571
C3-C4	1.3481	1.3546	1.3699/1.3702	1.4069/1.4065	1.4539/1.4538
C4-C4'			1.4289	1.3895	1.3532
Ru1-C1-C2	176.18	175.04	176.71/175.84	175.64/176.61	175.77/175.31
C1-C2-C3	178.99	179.17	178.77/178.59	177.33/178.87	178.22/177.15
C2-C3-C4	121.91	119.23	122.46/122.20	121.74/121.81	120.65/120.55
C3-C4-C4'			125.01/122.20	124.83/124.90	124.41/124.23

**Figure 6.** Plots (contours at $\pm 0.02 (e/\text{bohr}^3)^{1/2}$) of the frontier molecular (spin) orbitals of $[5a^{\dagger}]^{n+}$ ((a) $n = 0$; (b) $n = 1$; (c) $n = 2$), and spin density plot of $[5a^{\dagger}]^+$ (d).

Cyclic voltammetry measurements have revealed that complex **5a** undergoes two sequential one-electron oxidation processes ($E_{1/2}^1 = -0.62$ V; $E_{1/2}^2 = -0.37$ V vs. ferrocene/ferrocenium), generating $[5a]^+$ and $[5a]^{2+}$ (crystallographically characterised as the bis- PF_6 salt) [64]. These results, together with isolation of $[6a]^{n+}$ ($n = 0, 1, 2$) described here, point to the utility of the octa-3,5-diene-1,7-diynediyl ligand as a bridging structure in bimetallic com-

plexes, complementary in structure to octa-1,3,5,7-tetrayn-1,7-diyl but better able to support stable oxidation products. The DFT-optimised geometries of $[5a^\dagger]^+$ and $[5a^\dagger]^{2+}$ (Table 3) reveal a progressive evolution of the valence bond description of the bridging ligand towards more cumulated structures for the higher oxidation states. Thus, for $[5a^\dagger]^{n+}$, the Ru(1)–C(1), C(2)–C(3) and C(4)–C(4') bond lengths progressively decrease with increasing n , whilst the C(1)≡C(2) and C(3)=C(4) bond lengths increase. This structural progression is associated with a decrease in the calculated $\nu(\text{C}\equiv\text{C})$ wavenumbers ($\nu(\text{C}\equiv\text{C})/\text{cm}^{-1}$: $5a^\dagger$ 2024; $[5a^\dagger]^+$ 1904; $[5a^\dagger]^{2+}$ 1899), which is in agreement with experimental data from spectroelectrochemically generated samples ($\nu(\text{C}\equiv\text{C})/\text{cm}^{-1}$: $5a$ 2034; $[5a]^+$ 1939; $[5a]^{2+}$ 1920) [64]. Overall, the tendency for these octa-1,3,5,7-tetrayn-1,7-diyl-bridged bimetallic ruthenium complexes to evolve towards more structures featuring more cumulated bridging ligand structures on oxidation is a consequence of the substantial ligand character of the oxidation process, which in turn parallels the behaviour of polyyndiyl complexes of the 4d [27,37,72,74] and 5d [75–77] metals.

The UV-Vis-NIR spectrum of the deep red complex **5a** contains an intense absorption at ca. $19,417\text{ cm}^{-1}$, with several further high energy absorptions forming a large shoulder arising past $30,000\text{ cm}^{-1}$ (Figure 7). Similar visible absorption bands are also observed for other complexes of general form $[\{\text{Ru}(\text{dppe})\text{Cp}^*\}_2\{\text{C}\equiv\text{C}(\text{R})=\text{HC}-\text{CH}=(\text{R})\text{CC}\equiv\text{C}\}]$ (R = $\text{C}_6\text{H}_4\text{-SMe}$ (**5b**), $\text{C}_5\text{H}_4\text{N}$ (**5c**), $\text{C}_6\text{H}_4\text{-NO}_2$ (**5d**)), with the energy being sensitive to the electronic nature of the R group [64]. This observation clearly indicates that the conjugated bridging ligand plays a role in these transitions, and these optical features can therefore in turn provide an experimental reporter on changes to the electronic structure on a change in the redox state. As with the IR data, UV-Vis-NIR spectra of $[5a]^{n+}$ ($n = 0, 1, 2$) were collected via spectroelectrochemical methods, and data analysed with the aid of TD-DFT calculations carried out on $[5a^\dagger]^{n+}$ ($n = 0, 1, 2$) (Figures 7–12). In each case, analysis of the transitions revealed contributions from numerous molecular orbitals. To simplify the description of these spectra, interpretations were made on the basis of natural transition orbital (NTO) plots, generated for each associated ground (particle) to excited (hole) state transition.

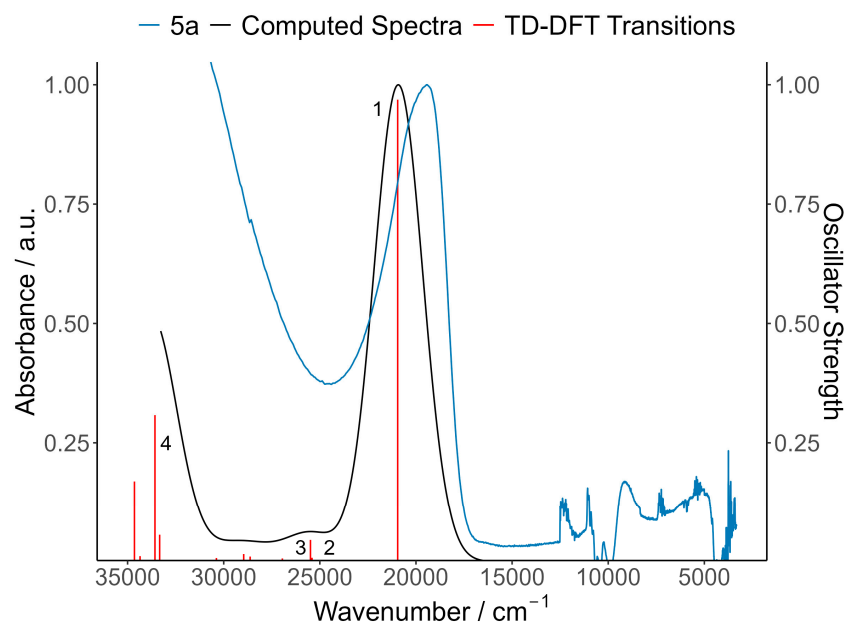


Figure 7. TD-DFT calculated UV-Vis-NIR spectrum of **5a** and associated transitions, with authentic SEC-UV-Vis-NIR generated spectrum overlay ($\text{CH}_2\text{Cl}_2/0.1\text{ M NBu}_4\text{PF}_6$).

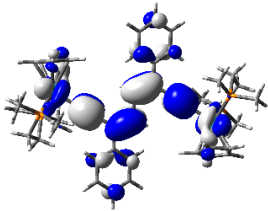
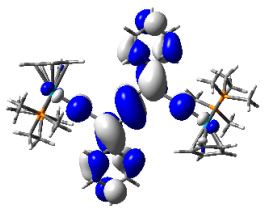
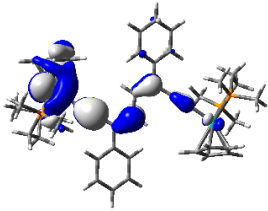
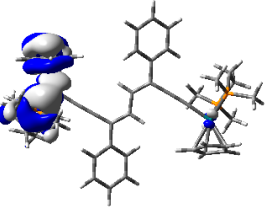
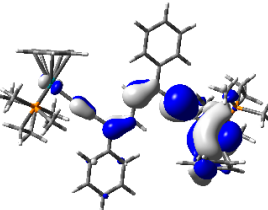
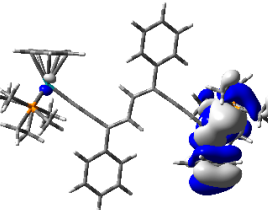
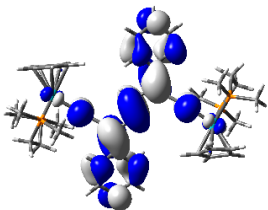
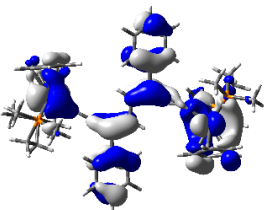
State	Transition/cm ⁻¹	Particle NTO	Hole NTO
1	Calc: 20,952 Obs: 19,417 <i>0.9687</i>		
2	Calc: 25,407 <i>0.0082</i>		
3	Calc: 25,488 <i>0.0453</i>		
4	Calc: 33,576 <i>0.308</i>		

Figure 8. Mapped isosurfaces showing particle and hole wavefunctions for NTO pairs for selected excited states of **5a**[†] (oscillator strength given in italic font).

For **5a**, the intense absorption observed at ca. 19,417 cm⁻¹ (515 nm) in CH₂Cl₂/0.1 M NBu₄PF₆ corresponds to a calculated transition in **5a**[†] at 20,952 cm⁻¹ ($f = 0.9687$) (Figure 7), and for which the NTO analysis (Figure 8) reveals significant transfer of electron density from the metals to ligand, allowing assignment as a metal-to-ligand charge-transfer (MLCT) band. This assignment is consistent with both the substantial solvatochromic behaviour of this transition in **5a**, and the significant shift to lower energy that tracks with the increasing electron-withdrawing character of the bridging ligand alkenyl substituents in complexes of general form $[\{\text{Ru}(\text{dppe})\text{Cp}^*\}_2\{\text{C}\equiv\text{CC}(\text{R})=\text{HC}-\text{CH}=(\text{R})\text{CC}\equiv\text{C}\}]$ (R = Ph, **5a**; C₆H₄-SMe, **5b**; C₅H₄N, **5c**; C₆H₄NO₂, **5d**) (Table 4).

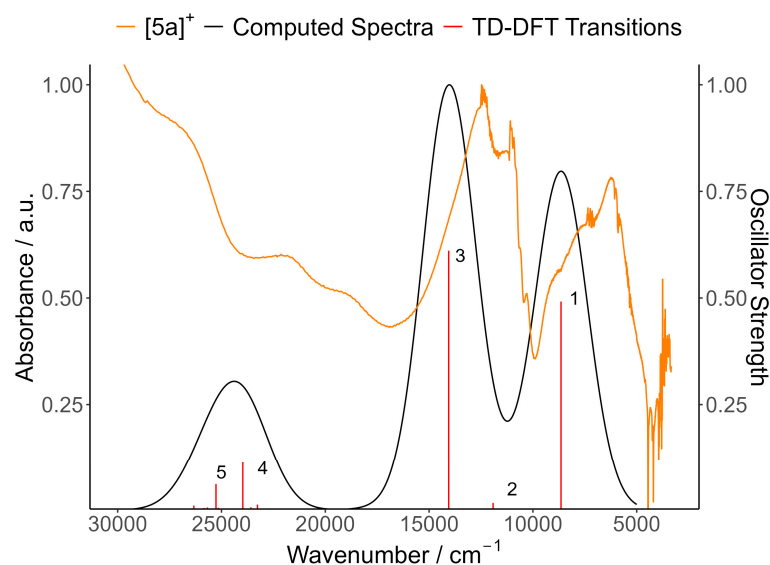


Figure 9. The TD-DFT calculated UV-Vis-NIR spectrum of $[5a]^+$ and associated transitions, overlaid on the authentic spectroelectrochemically generated UV-Vis-NIR spectrum of $[5a]^+$ ($CH_2Cl_2/0.1$ M NBu_4PF_6).

Table 4. Absorption maxima (λ) for **5a–d** and $[5a]^{n+}$ ($n = 1, 2$)/nm.

	<i>n</i> -Hexane	Cyclohexane	THF	CH_2Cl_2	PhCN
5a	476	496	511	513	520
5b	490	489	521	533	533
5c	516	525	555	562	549
5d	630	620	685	707	720

Less intense transitions are calculated for $5a^+$ at ca. $25,407\text{ cm}^{-1}$ ($f = 0.0082$) and $25,488\text{ cm}^{-1}$ ($f = 0.0453$) with the associated particle and hole states illustrating significant ligand-to-metal charge-transfer (LMCT) character. A transition of moderate intensity at ca. $33,576\text{ cm}^{-1}$ ($f = 0.3080$) has substantial intra-ligand $\pi-\pi^*$ character, accompanied by some charge transfer back to the metal centres.

The spectroelectrochemically generated UV-Vis-NIR spectrum of $[5a]^+$ contains three primary absorption band envelopes, although TD-DFT calculations indicate several mixed-transitions are responsible for the observed features (Figure 9). The consideration of all particle and hole wavefunctions shows the accumulation of spin density along the bridging ligand, supporting a strongly delocalised structure for the cationic species $[5a]^+$ (Figure 10). The relatively intense, low-energy band envelope observed at 6242 cm^{-1} in $[5a]^+$ corresponds to a calculated transition in $[5a^+]^+$ at 8646 cm^{-1} (Figure 9). This transition takes place between β -spin orbitals that are extensively delocalised over the 10-atom Ru_8Ru ($Ru-C\equiv C-C(Ph)=CH-CH=C(Ph)-C\equiv C-Ru$) chain and has significant $\pi-\pi^*$ character. This band may therefore be considered the ‘intervalence charge transfer’ (IVCT) band associated with the strongly delocalised (Class III) mixed-valent radical cation $[5a]^+$ that is perhaps better described as a charge resonance transition [78–80]. The intense absorption band envelopes between $12,000$ and $14,000\text{ cm}^{-1}$ in $[5a]^+$ correspond to a calculated transition in $[5a^+]^+$ at $14,056\text{ cm}^{-1}$ and arise from transitions in the α -spin manifold with a greater degree of metal-to-ligand charge-transfer (MLCT) character. Less intense transitions calculated at ca. $23,973\text{ cm}^{-1}$ and $25,265\text{ cm}^{-1}$ with mixed metal-to-ligand and intra-ligand charge-transfer character fit well to the heavily overlapped transitions that form the unresolved features through the visible region of the experimental spectrum (Figures 9 and 10).

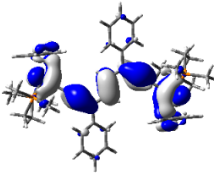
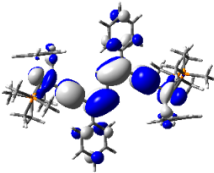
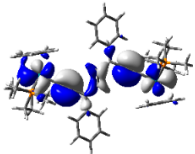
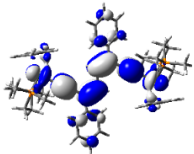
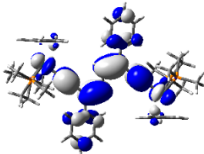
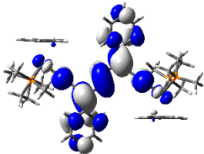
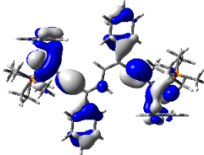
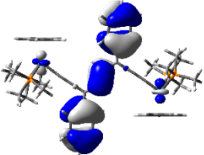
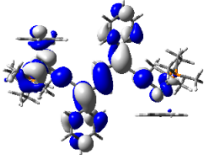
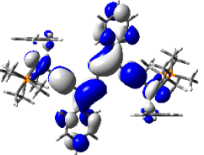
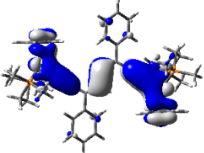
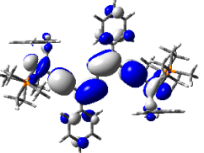
State	Transition/cm ⁻¹	Particle NTO		Hole NTO	
		α	β	α	β
1	Calc: 8646 Obs: 6242 <i>0.4916</i>				
2	Calc: 11,917 <i>0.0168</i>				
3	Calc: 14,056 Obs: 12,469 <i>0.6109</i>				
4	Calc: 23,973 Obs: 22,059 <i>0.1130</i>				
5	Calc: 25,265 <i>0.0614</i>				

Figure 10. Mapped isosurfaces showing particle and hole wavefunctions for NTO pairs for selected excited states of $[5a]^+$ (oscillator strength given in italic font).

The UV-Vis-NIR spectrum of the spectroelectrochemically generated dication $[5a][PF_6]_2$ contains a single intense absorption at $14,245\text{ cm}^{-1}$, with many overlapped, poorly resolved absorption bands at higher energy (Figure 11). The TD-DFT calculated spectrum reveals an additional band with a low-energy shoulder at ca. $30,000\text{ cm}^{-1}$. The intense absorption at $14,245\text{ cm}^{-1}$ observed for $[5a]^{2+}$ correlates well with the transition at $14,876\text{ cm}^{-1}$ calculated via TD-DFT methods for $[5a^+]^{2+}$ (Figure 11). The NTO analysis supports the description of this transition as an MLCT band. A less intense transition calculated at $26,675\text{ cm}^{-1}$ shows intra-ligand charge-transfer character from the pendant phenyl substituents to the octa-diene-diyldiyl fragment, whilst a second MLCT-like transition at $29,844\text{ cm}^{-1}$ also contributes to absorption in the visible region (Figure 12).

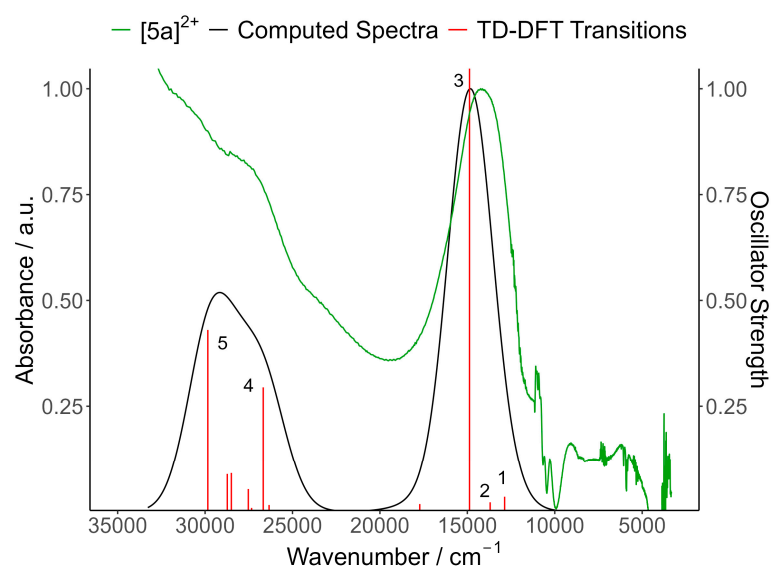


Figure 11. The TD-DFT calculated UV-Vis-NIR spectrum of $[5a]^{2+}$ and associated transitions, overlaid on the authentic spectroelectrochemically generated UV-Vis-NIR spectrum of $[5a]^{2+}$ ($\text{CH}_2\text{Cl}_2/0.1 \text{ M NBu}_4\text{PF}_6$).

State	Transition/ cm^{-1}	Particle NTO	Hole NTO
1	Calc: 12,869 0.0347		
2	Calc: 13,695 0.0216		
3	Calc: 14,876 Obs: 14,245 1.1536		

Figure 12. *Cont.*

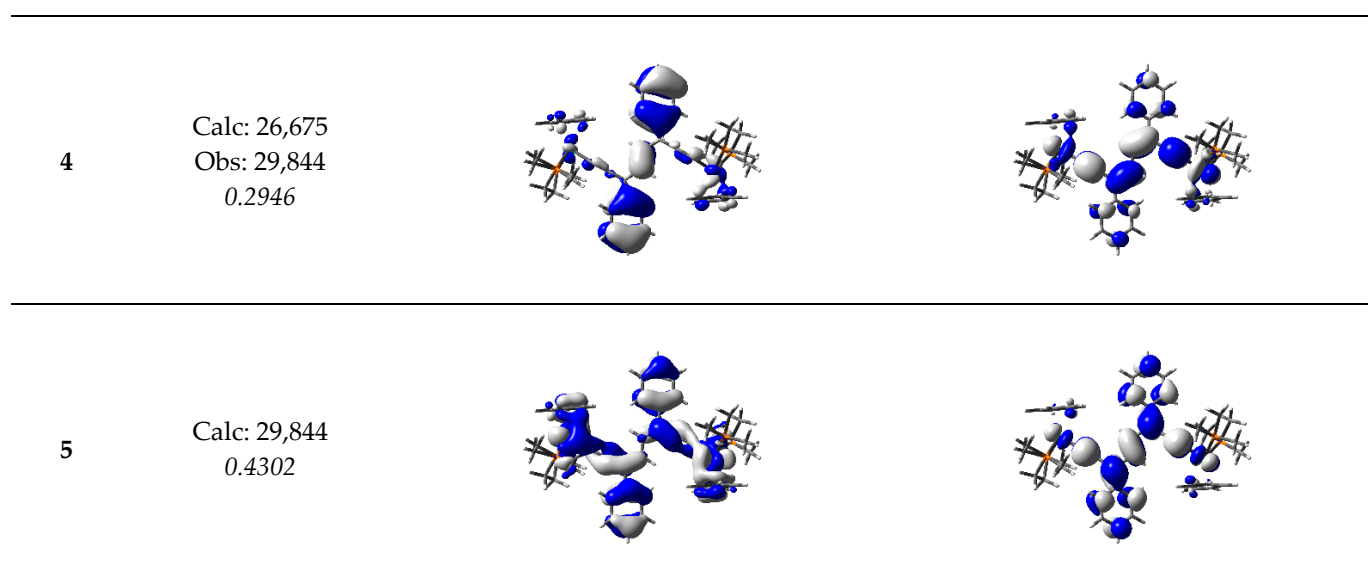


Figure 12. Mapped isosurfaces showing particle and hole wavefunctions for NTO pairs for selected excited states of $[5a][PF_6]_2$ (oscillator strength given in italic font).

Overall, the primary feature of the UV-Vis-NIR spectra of $[5a]^{n+}$ ($n = 0, 1, 2$) appears to be intense MLCT bands at 19,417 (**5a**), 12,000–14,000 ($[5a]^+$) and 14,245 ($[5a]^{2+}$), whilst $[5a]^+$ contains an additional IVCT or charge resonance band at ca. 6200 cm^{-1} . Additional transitions show significant accumulation of spin density to the bridging ligand and phenyl substituents in particular, supporting a strongly delocalised electronic structure.

3. Experimental Details

All reactions were performed under an atmosphere of nitrogen employing standard Schlenk techniques. Unless stated otherwise, no particular care was taken to exclude air upon work-up of reaction products. Solvents were dried by literature methods or by an Innovative Technologies Solvent Purification System and sparged with nitrogen before use. For chromatography, silica gel was used as received and alumina (basic) was oven dried ($100\text{ }^\circ\text{C}$) overnight before use. The compounds $[Ru\{C\equiv CC(R)=CH_2\}(dppe)Cp^*]$ ($R = \text{Ph}$ (**1a**), 4-MeS-C₆H₄ (**1b**)) [63], $[Ru\{C\equiv CC(R)=CH_2\}Cl(dppe)_2]$ ($R = \text{Ph}$ (**2a**), 4-MeS-C₆H₄ (**2b**)) [63], $[[Ru(dppe)Cp^*]_2\{\mu-C=C=C(\text{Ph})-H_2C-CH_2-C(\text{Ph})=C=C\}][PF_6]_2$ ($[3a][PF_6]_2$) [64] and $[FeCp_2]PF_6$ [81] were all prepared either in accordance with, or with slight refinements to, existing literature procedures. All other chemicals were purchased and used as received.

The various 1H , $^{13}C\{^1H\}$ and $^{31}P\{^1H\}$ spectra were recorded on Bruker 400 MHz (1H : 399.86 MHz, ^{13}C : 100.6 MHz, ^{31}P : 161.9 MHz), Bruker 500 MHz (1H : 500.10 MHz, ^{13}C : 125.8 MHz, ^{31}P : 202.4) and Bruker 600 MHz (1H : 600.10 MHz, ^{13}C : 150.9 MHz, ^{31}P : 242.9) spectrometers at room temperature. Chemical shifts are all reported relative to the residual solvent peaks. Unless stated otherwise $^{31}P\{^1H\}$, chemical shifts are reported relative to the NMR spectrometer lock signal. For all NMR spectra, multiplets are reported according to their closest first order approximation. For all NMR assignments, H_o , H_m and H_p refer to the *ortho*, *meta* and *para* protons of the phenyl rings of the ancillary phosphine ligands respectively, whilst C_i , C_o , C_m and C_p , similarly refer to the *ipso*, *ortho*, *meta* and *para* carbons of these same phenyl rings. IR spectra were recorded on an Agilent Cary 630 FTIR Spectrometer using ATR or in transmission mode from solutions between CaF₂ plates. Mass spectra were obtained from a Waters Liquid Chromatograph Premier Mass Spectrometer using positive-mode electrospray ionisation (ESI(+)) or atmospheric pressure chemical ionisation (APCI(+)). Samples were prepared in MeCN, EtOAc or MeOH and inserted by direct injection via the on-board injector.

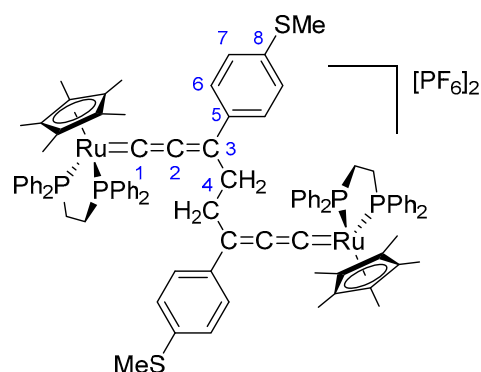
Single crystals of **2a_{ox}**, **2b_{ox}** and **[6a]PF₆** were used as supplied and mounted on a XtaLAB Synergy, Single source at home/near, HyPix diffractometer. All crystals were kept at a steady T = 100.0 K during data collection. Data were collected using Cu K α radiation ($\lambda = 1.54184 \text{ \AA}$). The structures were solved, and the space group determined by the ShelXT 2018/2 structure solution program using dual methods and refined by full matrix least-squares minimisation on F^2 using version 2018/3 of XL [82,83], while using Olex2 1.5 [84,85] or WinGX 2018.3 [86] as graphical interfaces. For all structures, all non-hydrogen atoms were refined anisotropically. Hydrogen atom positions were calculated geometrically and refined using the riding model. Disordered phenyl groups in **2b_{ox}** were refined as rigid fragments, with thermal similarity constraints, while the PF₆ group in **[6a]PF₆** was refined with 1,2 similarity restraints on the P-F bonds due to disorder of the F-atoms in the equatorial plane. Crystallographic data for the structures reported in this paper have been deposited at the Cambridge Crystallographic Data Centre (2307001-2307003).

DFT calculations were carried out using the Gaussian09 suite of programs (revision A.02) [87], and the results analysed with the aid of GaussView5.0 and GassSum3.0 [88]. All calculations were carried out with the BLYP35 functional [5], with the LANL2DZ basis set for Ru [89–91] and 6-31G** for all other atoms [92,93], and a COSMO(CH₂Cl₂) solvent model [94,95]. All optimised structures were confirmed as true minima through the absence of imaginary frequencies. Reported values of vibrational frequencies have been scaled by a factor of 0.93 [70], with descriptions of the optical spectra performed within the framework of natural transition orbital analyses [96].

Cyclic voltammetry measurements were performed in CH₂Cl₂ solutions containing 0.1 M NBu₄PF₆-supporting electrolyte using a platinum working electrode and a PalmSens Emstat2+ or Emstat3+ potentiostat. Potential measurements were referenced against an internal ferrocene/ferrocenium (FeCp₂/[FeCp₂]⁺) couple reference.

Spectroelectrochemistry was conducted in an OTTLE cell of Hartl design [97] using CH₂Cl₂ solutions containing 0.1 M NBu₄PF₆-supporting electrolyte. Spectra were recorded on an Agilent Technologies Cary 660 FTIR. Electrolysis in the cell was performed using a PalmSens Emstat3+ potentiostat at a scan rate of 0.0025 V s⁻¹.

3.1. Synthesis of $\{[Ru(dppe)Cp^*]_2\{\mu-C=C=C(MeS-4-C_6H_4)-H_2C-CH_2-C(MeS-4-C_6H_4)=C=C\}\} [PF_6]_2$ (**3b**)[PF₆]₂

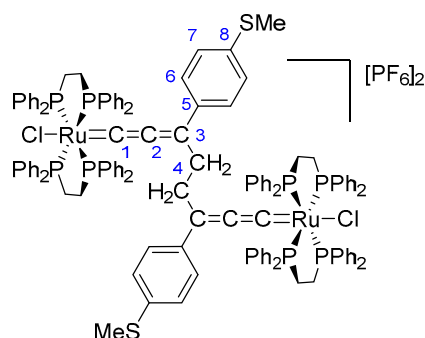


A solution of **1b** (0.16 g, 0.20 mmol) in CH₂Cl₂ (5 mL) was cooled to $-78 \text{ }^\circ\text{C}$ after which it was treated with [FeCp₂]PF₆ (0.061 g, 0.18 mmol) and stirred for 2 h. The solvent volume was reduced, and the concentrated solution filtered into stirred hexanes, giving the title product as a purple powder (0.160 g, 0.099 mmol, 98%).

¹H NMR (CDCl₃ 400 MHz) δ /ppm: 7.51–7.50 (m, 2H, H_{6/7}); 7.47–7.45 (m, 4H, H_o, dppe); 7.36–7.28 (m, 8H, H_o + H_p, dppe); 7.17–7.12 (m, 4H, H_m, dppe); 2.82 (m, 2H, dppe); 2.62 (m, 2H, dppe); 2.50 (s, 3H, SMe); 1.93 (s, 2H, H₄); 1.59 (s, 15H, Me of Cp*). ¹³C{¹H} NMR (CDCl₃ 100.6 MHz) δ /ppm: 287.8–287.5 (m, C₁); 198.4 (s, C₂); 156.0 (s, C₃); 146.9 (s, C₈); 139.1 (s, C₅); 134.7–134.2 (m, 2 \times C_i, dppe); 132.7–132.6 (app t., C_o, dppe); 132.5–132.4 (app t., C_o, dppe); 131.4 (s, C_p, dppe); 131.3 (s, C_p, dppe); 128.9–128.8 (app t., C_m, dppe); 128.7–128.6 (app t., C_m, dppe); 127.5 (s, C_{6/7}); 125.7 (s, C_{6/7}); 102.3 (s, Cp*); 40.2 (s, C₄); 30.5–

30.0 (m, dppe); 14.7 (s, SMe); 10.2 (s, Cp^{*}). ³¹P{¹H} NMR (CDCl₃ 161.9 MHz) δ/ppm: 78.76 (s, dppe); −144.81 (sept, PF₆[−]). IR ATR ν/cm^{−1}: 1917 ν(C=C=C); 834 ν(PF₆[−]). ESI(+)-MS *m/z*: Calculated for [M]²⁺ ([C₉₄H₉₆P₄S₂Ru₂]²⁺) = 807.1912. Observed: 807.1918 [M]²⁺.

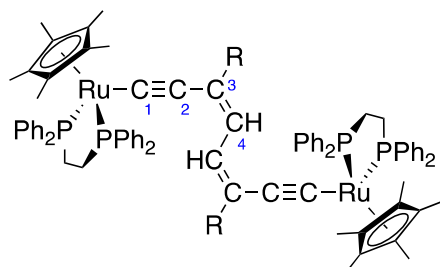
3.2. Synthesis of $\{[RuCl(dppe)_2]_2\{\mu-C=C=C(MeS-4-C_6H_4)-H_2C-CH_2-C(MeS-4-C_6H_4)=C=C\}\}[PF_6]_2$ (**4b**)[PF₆]₂)



A solution of **2b** (0.097 g, 0.088 mmol) in CH₂Cl₂ (5 mL) was cooled to −78 °C after which it was treated with [FeCp₂]₂PF₆ (0.031 g, 0.094 mmol) and stirred for 2 h. The solvent volume was reduced and the concentrated solution filtered into stirred hexanes, giving the title product as a dark purple powder (0.095 g, 0.043 mmol, 97%). Extremely poor solubility prevented informative ¹³C{¹H} measurements from being performed.

¹H NMR (CD₂Cl₂ 500 MHz) δ/ppm: 7.32–6.99 (m, 40H, dppe); 6.71 (m, 2H, H_{6/7}); 6.49 (m, 2H, H_{6/7}); 3.16 (m, 4H, dppe); 2.78 (m, 4H, dppe); 2.50 (s, 3H, SMe); 1.92 (s, 2H, H₄). ³¹P{¹H} NMR (CD₂Cl₂ 161.9 MHz) δ/ppm: 40.41 (s, dppe); −144.81 (sept, PF₆[−]). IR ATR ν/cm^{−1}: 1915 ν(C=C=C); 835 ν(PF₆[−]). ESI(+)-MS *m/z*: Calculated for [M]²⁺ ([C₁₂₆H₁₁₄Cl₂P₈S₂Ru₂]²⁺) = 1106.1858. Observed: 1106.1789 [M]²⁺.

3.3. Synthesis of $\{[Ru(dppe)Cp^*]_2\{\mu-C\equiv CC(R)=HC-CH=C(R)C\equiv C\}\}$ (R = Ph (**5a**), MeS-4-C₆H₄ (**5b**))



5a (R = Ph); **5b** (R = 4-SMe-C₆H₄)

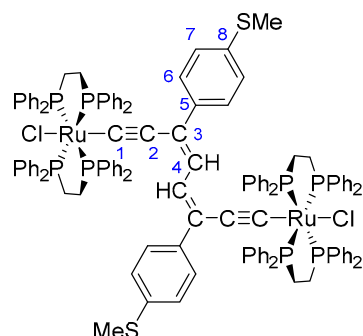
A solution of [**3a**]₂[PF₆]₂ or [**3b**]₂[PF₆]₂ (ca. 0.06 mmol) in THF (5 mL) was treated with *t*-BuOK (2.5 equiv., ca. 0.17 mmol) and stirred for 2 h. Removal of solvent under reduced pressure was followed by passage of a CH₂Cl₂ extract through a basic alumina plug. The solid obtained after taking the eluted fraction to dryness was triturated with hexanes gave the title products as red-orange powders in near-quantitative yield.

5a: data were in accord with previous reports of an authentic sample [64].

5b: ¹H NMR (CDCl₃ 400 MHz) δ/ppm: 7.71–7.70 (m, 4H, H_o, dppe); 7.34–7.15 (m, 16H, H_o + H_p + H_m, dppe); 6.94 (s, 1H, H₄); 6.77 (app d., J_{HH} = 8.0 Hz, 2H, H_{6/7}); 6.64 (app d., J_{HH} = 8.0 Hz, 2H, H_{6/7}); 2.76 (m, 2H, dppe); 2.39 (s, 3H, SMe); 2.09 (m, 2H, dppe); 1.57 (s, 15H, Me of Cp^{*}). ¹³C{¹H} NMR (CDCl₃, 100.6 MHz) δ/ppm: 133.6–133.5 (m, C_o, dppe); 133.3–133.2 (m, C_o, dppe); 129.1 (s, C_p, dppe); 129.0 (s, C_p, dppe); 127.6–127.4 (m, 2 × C_m, dppe); 93.0 (s, Cp^{*}); 30.5 (m, dppe); 10.4 (s, Me of Cp^{*}). * Limited solubility prevented observation of C₁, C₂, C₃ and C₄ ¹³C{¹H} resonances. ³¹P{¹H} NMR (CDCl₃ 161.9 MHz)

δ /ppm: 81.95 (s, dppe). IR ATR ν /cm⁻¹: 2027 ν (C≡C). ESI(+)-MS m/z : Calculated for [M]⁺ ([C₉₄H₉₄P₄S₂Ru₂)⁺) = 1614.3834. Observed: 1614.3862 [M]⁺.

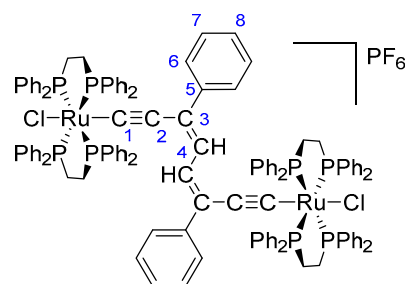
3.4. Synthesis of [{RuCl(dppe)}₂]{ μ -C≡CC(MeS-4-C₆H₄)=HC-CH=C(MeS-4-C₆H₄)C≡C} (6b)



A solution of [4b][PF₆]₂ (0.097 g, 0.039 mmol) in THF (5 mL) was treated with *t*-BuOK (0.011 g, 0.098 mmol) and stirred for 2 h. Removal of solvent under reduced pressure, followed by passage through a basic alumina plug and trituration of the solid obtained from the eluted fraction with hexanes gave the title product as a red-brown powder (0.044 g, 0.020 mmol, 51%).

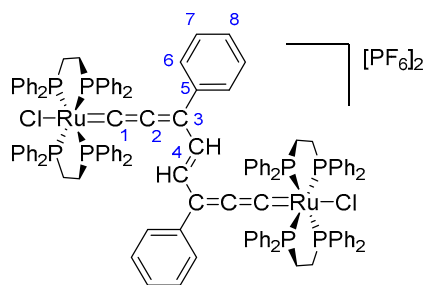
¹H NMR (CDCl₃ 400 MHz) δ /ppm: 7.71 (m, 8H, H_o, dppe); 7.19–7.11 (m, 8H, H_o, dppe); 7.10–7.00 (m, 8H, H_p, dppe); 6.97–6.90 (m, 21H, H₆ + H₇ + H₄ + H_m, dppe); 2.76 (m, 4H, dppe); 2.58 (m, 4H, dppe); 2.44 (s, 3H, SMe). ¹³C{¹H} NMR (CDCl₃ 100.6 MHz) δ /ppm: 136.7–136.0 (m, 4 × C_i); 135.0–134.9 (m, C_o, dppe); 134.6 (); 134.3–134.2 (m, C_o, dppe); 133.9 (); 129.3 (s, C_p, dppe); 128.6 (s, C_p, dppe); 127.5–127.4 (m, C_m, dppe); 127.2 (s, C_{6/7}); 127.0–126.9 (m, C_m, dppe); 126.3 (s, C_{6/7}); 30.8–30.6 (m, dppe); 22.8 (s, SMe). Poor solubility prevented assignment of several ¹³C{¹H} NMR resonances. ³¹P{¹H} NMR (CDCl₃ 161.9 MHz) δ /ppm: 49.74 (s, dppe). IR ATR ν /cm⁻¹: 2035 ν (C≡C). ESI(+)-MS m/z : Calculated for [M-Cl⁻ + MeCN]⁺ ([C₁₂₈H₁₁₅ClNP₈S₂Ru₂)⁺) = 2216.4147. Observed: 2216.4173 [M-Cl⁻ + MeCN]⁺.

3.5. Synthesis of [{RuCl(dppe)}₂]{ μ -C≡CC(Ph)=HC-CH=C(Ph)C≡C}PF₆ ([6a]PF₆)



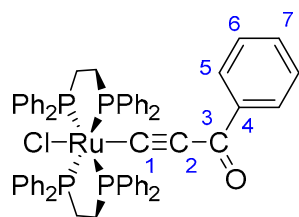
A solution of 2a (0.098 g, 0.092 mmol) in CH₂Cl₂ (10 mL) was cooled to -78 °C and then treated with [FeCp₂]⁺PF₆⁻ (0.061 g, 0.18 mmol) and stirred for 2 h, after which the solution was allowed to reach room temperature before *t*-BuOK (2.2 equiv.) was added. The solvent volume was reduced, and the concentrated solution filtered into stirred hexanes, giving the title product as a green-brown powder (0.062 g, 0.027 mmol, 30%). Single crystals suitable for X-ray diffraction were obtained by layering a CH₂Cl₂ solution of [6a]PF₆ with MeOH. Low solubility and the inherent paramagnetism of the sample prevented a satisfactory ¹³C{¹H} NMR spectrum from being obtained.

¹H NMR (CDCl₃ 500 MHz) δ /ppm: 8.14–6.93 (m, 45H, dppe + Ph); 6.44 (s, 1H, H₄); 2.68 (m, 4H, dppe); 2.58 (m, 4H, dppe). ³¹P{¹H} NMR (CDCl₃ 202.4 MHz) δ /ppm: 78.76 (s, dppe); -144.81 (sept, PF₆⁻). IR ATR ν /cm⁻¹: 1918 ν (C=C=C); 833 ν (PF₆⁻). ESI(+)-MS m/z : Calculated for [M-H - 2 × Cl⁻ + MeOH + MeCN]⁺ ([C₁₂₇H₁₁₄NOP₈Ru₂)²⁺) = 2120.4888. Observed: 2120.3842 [M-H - 2 × Cl⁻ + MeOH + MeCN]⁺.

3.6. Preparation of $[\{RuCl(dppe)_2\}_2\{\mu-C=C=C(Ph)-HC=CH-C(Ph)=C=C\}][PF_6]_2$ (**6a**)[PF₆]₂)

A solution of **2a** (0.102 g, 0.096 mmol) in CH₂Cl₂ (10 mL) was cooled to -78 °C and then treated with [FeCp₂]₂PF₆ (0.091 g, 0.27 mmol) and stirred for 2 h, after which the solution was allowed to reach room temperature before *t*-BuOK (2.2 equiv.) was added. The solvent was reduced and the concentrated solution filtered into stirred hexanes, giving the title product as a blue powder (0.044 g, 0.018 mmol, 19%).

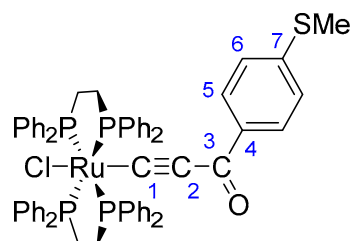
¹H NMR (CDCl₃ 600 MHz) δ /ppm: 7.54–7.03 (m, 45H, dppe + Ph); 6.30 (s, 1H, H₄); 3.01 (m, 4H, dppe); 2.89 (m, 4H, dppe). ¹³C{¹H} NMR (CDCl₃ 150.9 MHz) δ /ppm: 214.3 (s, C₂); 161.2 (s, C₃); 136.6–135.3 (m, C_i, dppe); 134.2 (m, C_o, dppe); 133.9 (s, Ph); 133.2 (m, C_o, dppe); 132.5 (s, Ph); 131.5 (s, C_p, dppe); 131.2 (s, C_p, dppe); 128.8 (m, C_m, dppe); 128.7 (s, Ph); 128.2 (s, C_m, dppe); 126.9 (s, Ph); 29.3–29.0 (m, dppe). C₁ was not observed due to poor solubility. ³¹P{¹H} NMR (CDCl₃ 242.9 MHz) δ /ppm: 40.42 (s, dppe); -147.94 (sept, PF₆). IR ATR ν /cm⁻¹: 1899 ν (C=C=C); 831 ν (PF₆⁻). ESI(+)-MS *m/z*: Calculated for [M]²⁺ ([C₁₂₄H₁₁₀Cl₂P₈Ru₂]²⁺) = 1060.1981. Observed: 1060.1921 [M]²⁺.

3.7. Preparation of *trans*-[Ru(C≡CC(=O)Ph)Cl(dppe)₂] (**2a_{ox}**)

This compound was obtained from aerial oxidation of a solid sample of **2a** stored under ambient conditions, purified by preparative TLC (acetone/hexanes 3:7) and obtained as a yellow solid. Single crystals suitable for X-ray diffraction were grown by layering a CH₂Cl₂ solution of **2a_{ox}** with MeOH.

¹H NMR (CDCl₃ 400 MHz) δ /ppm: 7.40–7.38 (m, 8H, H_o, dppe); 7.29–7.24 (m, 8H, H_o, dppe); 7.22–7.21 (m, 6H, H_p + Ph); 7.07–7.03 (m, 12H, H_p + H_m, dppe); 6.98–6.94 (m, 2H, Ph); 6.89–6.85 (m, 8H, H_m, dppe); 2.92 (m, 4H, dppe); 2.81 (m, 4H, dppe). ¹³C{¹H} NMR (CDCl₃ 100.6 MHz) δ /ppm: 173.5 (s, C₃); 139.1 (s, C₄); 135.9–135.4 (m, 2 × C_i, dppe); 134.6–134.5 (m, C_o, dppe); 134.0–133.9 (m, C_o, dppe); 130.7 (s, C_{Ph}); 129.4 (s, C_{Ph}); 129.3 (s, C_p, dppe); 127.6–127.5 (m, C_m, dppe); 127.4 (s, C_{Ph}); 127.3–127.2 (m, C_m, dppe); 120.8 (s, C₂); 30.8–30.3 (m, dppe). ³¹P{¹H} NMR (CDCl₃ 161.9 MHz) δ /ppm: 47.09 (s, dppe). IR ATR ν /cm⁻¹: 2000 ν (C≡C); 1705 ν (C=O). ESI(+)-MS *m/z*: Calculated for [M-Cl⁻ + MeCN]⁺ ([C₆₃H₅₆NO₄Ru]⁺) = 1068.2356. Observed: 1068.2341 [M-Cl⁻ + MeCN]⁺.

3.8. Preparation of *trans*-[Ru{C≡CC(=O)-4-MeS-C₆H₄}Cl(dppe)₂] (**2b_{ox}**)



This compound was obtained from aerial oxidation of a solid sample of **2b** stored under ambient conditions, purified by preparative TLC (acetone/hexanes 3:7) and obtained as a yellow solid. Single crystals suitable for X-ray diffraction were grown by layering a CH₂Cl₂ solution of **2b_{ox}** with MeOH.

¹H NMR (CDCl₃ 400 MHz) δ/ppm: 7.41–7.39 (m, 8H, H_o, dppe); 7.24–7.20 (m, 8H, H_o, dppe); 7.09 (app d., J_{HH} = 8.5 Hz, 2H, H_{5/6}); 7.05–7.02 (m, 16H, H_p + H_m, dppe); 6.88 (app t, J_{HH} = 7.6 Hz, 8H, H_m, dppe); 6.76 (app d, J_{HH} = 8.5 Hz, 2H, H_{5/6}); 2.92 (m, 4H, dppe); 2.79 (m, 4H, dppe); 2.45 (s, 3H, SMe). ¹³C{¹H} NMR (CDCl₃ 100.6 MHz) δ/ppm: 195.2 (s, C₃); 142.1 (s, C₄); 136.0–135.4 (m, 2 × C_i, dppe); 134.6 (m, C_o, dppe); 133.9 (m, C_o, dppe); 129.7 (s, C_{5/6}); 129.3 (s, C_p, dppe); 129.2 (s, C_p, dppe); 127.6 (m, C_m, dppe); 127.3 (m, C_m, dppe); 126.6 (s, C₂); 124.3 (s, C_{5/6}); 29.9 (m, dppe); 15.3 (s, SMe). ³¹P{¹H} NMR (CDCl₃ 161.9 MHz) δ/ppm: 46.92 (s, dppe). IR ATR ν/cm⁻¹: 1998 ν(C≡C); 1704 ν(C=O). ESI(+)-MS *m/z*: Calculated for [M-Cl⁻ + MeCN]⁺ ([C₆₄H₅₈NOP₄SRu]⁺) = 1114.2233. Observed: 1114.2227 [M-Cl⁻ + MeCN]⁺.

4. Conclusions

The dinuclear octa-3,5-diene-1,7-diyndiyl-bridged complexes [{Ru}₂{μ-C≡CC(R)=CH-HC=(R)CC≡C}] ([Ru] = Ru(dppe)Cp* (**5a,b**); {Ru} = RuCl(dppe)₂ (**6a,b**)) have been prepared via the one-electron oxidation of alkenylacetylide complexes [Ru{C≡CC(R)=CH₂}(dppe)Cp*] (**1**) and [Ru{C≡CC(R)=CH₂}Cl(dppe)₂] (**2**) (R = Ph (**a**); R = 4-MeS-C₆H₄ (**b**)) and deprotonation of the resultant ethane-bridged dinuclear bis(allylenylidene) complexes [{Ru}₂{μ-C=C=C(R)-CH₂-H₂C-(R)C=C=C}] [PF₆]₂ ({Ru} = Ru(dppe)Cp* ([**3a,b**][PF₆]₂); {Ru} = RuCl(dppe)₂ ([**4a,b**][PF₆]₂)), formed by C_δ-C_{δ'} homo-dimerisation of [**1**]⁺ or [**2**]⁺, respectively. The chemical reactivity profiles and redox/electrochemical response of **1** (and by inference **2**) and **5** (and by inference **6**), coupled with spectroscopic and (TD-)DFT calculations, support a number of important conclusions, which were explored with the more soluble {Ru(dppe)Cp*}-based complexes **1** and **5** and the computational model systems [Ru{C≡CC(Ph)=CH₂}(dmpe)Cp] (**1a**[†]) and [{Ru(dmpe)Cp}₂{μ-C≡CC(Ph)=CH-CH(Ph)CC≡C}] (**5a**[†]). Oxidation of the alkenylacetylide complex **1** and **2** results in the accumulation of significant radical character at C_δ, rationalising the formation of the new C-C bond in [**3**][PF₆]₂ and [**4**][PF₆]₂. After deprotonation, the resulting octa-3,5-diene-1,7-diyndiyl are found to undergo a sequence of two, facile one-electron oxidation steps to give the redox series [**5**]^{*n*+} and [**6**]^{*n*+} (*n* = 0, 1, 2). The greater stability of the one- and two-electron oxidation products permit a range of more detailed investigations than are possible with similar octa-1,3,5,7-tetraiyndiyl complexes. A combination of crystallographic characterisation, spectroelectrochemical study and (TD-)DFT calculations indicate a significant degree of charge delocalisation and ligand redox non-innocence for the dinuclear complexes [**5**]^{*n*+} (and hence [**6**]^{*n*+}). The formally mixed-valence one-electron oxidised species are assigned as Robin-Day Class III or fully delocalised species.

Author Contributions: Conceptualization, P.J.L. and M.R.H.; methodology, M.R.H., S.A.M. and P.J.L.; formal analysis, M.R.H., S.A.M. and P.J.L.; investigation, M.R.H.; resources, S.A.M. and P.J.L.; data curation, M.R.H., S.A.M. and P.J.L.; writing—original draft preparation, M.R.H.; writing—review and editing, M.R.H., S.A.M. and P.J.L.; supervision, P.J.L.; project administration, P.J.L.; funding

acquisition, M.R.H., S.A.M. and P.J.L. All authors have read and agreed to the published version of the manuscript.

Funding: This work was funded by the University of Western Australia through a Dean's Scholarship for Excellence to M.R.H and the Australian Research Council through a Future Fellowship to S.A.M. (FT200100243).

Data Availability Statement: The data presented in this study are available in the article.

Acknowledgments: M.R.H. held a Dean's Excellence in Science Ph.D. Scholarship from the Faculty of Science, University of Western Australia. S.A.M. thanks the Australian Research Council (ARC) for a Future Fellowship (FT200100243). The authors gratefully acknowledge the facilities and the scientific and technical assistance of Microscopy Australian at the Centre for Microscopy, Characterisation Analysis, the University of Western Australia, a facility funded by the University, State, and Commonwealth Governments.

Conflicts of Interest: The authors declare no conflict of interest.

References

1. Aguirre-Etcheverry, P.; O'Hare, D. Electronic Communication through Unsaturated Hydrocarbon Bridges in Homobimetallic Organometallic Complexes. *Chem. Rev.* **2010**, *110*, 4839–4864. [[CrossRef](#)] [[PubMed](#)]
2. Launay, J.P. Long-distance intervalence electron transfer. *Chem. Soc. Rev.* **2001**, *30*, 386–397. [[CrossRef](#)]
3. Launay, J.P. Mixed-Valent Compounds and their Properties—Recent Developments. *Eur. J. Inorg. Chem.* **2020**, *2020*, 329–341. [[CrossRef](#)]
4. Launay, J.P. An orbital approach of electron transfer in multisite systems. Implications for carbon-rich spacers. *Polyhedron* **2015**, *86*, 151–166. [[CrossRef](#)]
5. Renz, M.; Theilacker, K.; Lambert, C.; Kaupp, M. A Reliable Quantum-Chemical Protocol for the Characterization of Organic Mixed-Valence Compounds. *J. Am. Chem. Soc.* **2009**, *131*, 16292–16302. [[CrossRef](#)] [[PubMed](#)]
6. Fitzgerald, E.C.; Brown, N.J.; Edge, R.; Helliwell, M.; Roberts, H.N.; Tuna, F.; Beeby, A.; Collison, D.; Low, P.J.; Whiteley, M.W. Orbital Symmetry Control of Electronic Coupling in a Symmetrical, All-Carbon-Bridged "Mixed Valence" Compound: Synthesis, Spectroscopy, and Electronic Structure of $[\{\text{Mo}(\text{dppe})(\eta\text{-C}_7\text{H}_7)\}_2(\mu\text{-C}_4)]^{n+}$ ($n = 0, 1, \text{ or } 2$). *Organometallics* **2012**, *31*, 157–169. [[CrossRef](#)]
7. Pieslinger, G.E.; Aramburu-Troselj, B.M.; Cadranel, A.; Baraldo, L.M. Influence of the Electronic Configuration in the Properties of $d^6\text{-}d^5$ Mixed-Valence Complexes. *Inorg. Chem.* **2014**, *53*, 8221–8229. [[CrossRef](#)] [[PubMed](#)]
8. Gückel, S.; Safari, P.; Ghazvini, S.M.B.H.; Hall, M.R.; Gluyas, J.B.G.; Kaupp, M.; Low, P.J. Iron Versus Ruthenium: Evidence for the Distinct Differences in the Electronic Structures of Hexa-1,3,5-triyn-1,6-diyl-bridged Complexes $[\text{Cp}^*(\text{dppe})\text{M}]\{\mu\text{-}(\text{C}\equiv\text{C})_3\}\{\text{M}(\text{dppe})\text{Cp}^*\}^+$ ($\text{M} = \text{Fe, Ru}$). *Organometallics* **2021**, *40*, 346–357. [[CrossRef](#)]
9. Launay, J.P. Electron transfer in molecular binuclear complexes and relation with electron transport through nanojunctions. *Coord. Chem. Rev.* **2013**, *257*, 1544–1554. [[CrossRef](#)]
10. Zhang, J.; Ouyang, J.; Ye, Y.X.; Li, Z.; Lin, Q.; Chen, T.; Zhang, Z.; Xiang, S.C. Mixed-Valence Cobalt(II/III) Metal–Organic Framework for Ammonia Sensing with Naked-Eye Color Switching. *ACS Appl. Mater. Interfaces* **2018**, *10*, 27465–27471. [[CrossRef](#)]
11. Corrente, G.A.; Cospito, S.; Capodilupo, A.L.; Beneduci, A. Mixed-Valence Compounds as a New Route for Electrochromic Devices with High Coloration Efficiency in the Whole Vis-NIR Region. *Appl. Sci.* **2020**, *10*, 8372. [[CrossRef](#)]
12. Ma, X.; Pang, C.; Li, S.; Li, J.; Wang, M.; Xiong, Y.; Su, L.; Luo, J.; Xu, Z.; Lin, L. Biomimetic Synthesis of Ultrafine Mixed-Valence Metal–Organic Framework Nanowires and Their Application in Electrochemiluminescence Sensing. *ACS Appl. Mater. Interfaces* **2021**, *13*, 41987–41996. [[CrossRef](#)] [[PubMed](#)]
13. Jiao, J.; Long, G.J.; Rebbouh, L.; Grandjean, F.; Beatty, A.M.; Fehlner, T.P. Properties of a Mixed-Valence $(\text{Fe}^{\text{II}})_2(\text{Fe}^{\text{III}})_2$ Square Cell for Utilization in the Quantum Cellular Automata Paradigm for Molecular Electronics. *J. Am. Chem. Soc.* **2005**, *127*, 17819–17831. [[CrossRef](#)] [[PubMed](#)]
14. Gluyas, J.B.G.; Gückel, S.; Kaupp, M.; Low, P.J. Rational Control of Conformational Distributions and Mixed-Valence Characteristics in Diruthenium Complexes. *Chem. Eur. J.* **2016**, *22*, 16138–16146. [[CrossRef](#)] [[PubMed](#)]
15. Parthey, M.; Gluyas, J.B.G.; Fox, M.A.; Low, P.J.; Kaupp, M. Mixed-Valence Ruthenium Complexes Rotating through a Conformational Robin-Day Continuum. *Chem. Eur. J.* **2014**, *20*, 6895–6908. [[CrossRef](#)] [[PubMed](#)]
16. Costuas, K.; Cador, O.; Justaud, F.; Le Stang, S.; Paul, F.; Monari, A.; Evangelisti, S.; Toupet, L.; Lapinte, C.; Halet, J.F. 3,5-Bis(ethynyl)pyridine and 2,6-Bis(ethynyl)pyridine Spanning Two $\text{Fe}(\text{Cp}^*)(\text{dppe})$ Units: Role of the Nitrogen Atom on the Electronic and Magnetic Couplings. *Inorg. Chem.* **2011**, *50*, 12601–12622. [[CrossRef](#)]
17. Fitzgerald, E.C.; Ladjarafi, A.; Brown, N.J.; Collison, D.; Costuas, K.; Edge, R.; Halet, J.F.; Justaud, F.; Low, P.J.; Meghezzi, H.; et al. Spectroscopic Evidence for Redox Isomerism in the 1,4-Diethynylbenzene-Bridged Heterobimetallic Cation $[\{\text{Fe}(\text{dppe})\text{Cp}^*\}(\mu\text{-}\text{C}\equiv\text{CC}_6\text{H}_4\text{C}\equiv\text{C})\{\text{Mo}(\text{dppe})(\eta\text{-C}_7\text{H}_7)\}]\text{PF}_6$. *Organometallics* **2011**, *30*, 4180–4195. [[CrossRef](#)]

18. Zhang, J.; Zhang, M.X.; Sun, C.F.; Xu, M.; Hartl, F.; Yin, J.; Yu, G.A.; Rao, L.; Liu, S.H. Diruthenium Complexes with Bridging Diethynyl Polyaromatic Ligands: Synthesis, Spectroelectrochemistry, and Theoretical Calculations. *Organometallics* **2015**, *34*, 3967–3978. [[CrossRef](#)]
19. Bruce, M.; Low, P. Transition metal complexes containing all-carbon ligands. *Adv. Organomet. Chem.* **2004**, *50*, 179–444.
20. Halet, J.F.; Lapinte, C. Charge delocalization vs localization in carbon-rich iron mixed-valence complexes: A subtle interplay between the carbon spacer and the (dppe)Cp*Fe organometallic electrophore. *Coord. Chem. Rev.* **2013**, *257*, 1584–1613. [[CrossRef](#)]
21. Zheng, Q.L.; Schneider, J.F.; Amini, H.; Hampel, F.; Gladysz, J.A. Wire like diplatinum, triplatinum, and tetraplatinum complexes featuring X[PtC≡CC≡CC≡CC≡C]_mPtX segments; iterative syntheses and functionalization for measurements of single molecule properties. *Dalton Trans.* **2019**, *48*, 5800–5816. [[CrossRef](#)] [[PubMed](#)]
22. Ballmann, S.; Hieringer, W.; Secker, D.; Zheng, Q.L.; Gladysz, J.A.; Gorling, A.; Weber, H.B. Molecular Wires in Single-Molecule Junctions: Charge Transport and Vibrational Excitations. *ChemPhysChem* **2010**, *11*, 2256–2260. [[CrossRef](#)] [[PubMed](#)]
23. Szafert, S.; Paul, F.; Meyer, W.E.; Gladysz, J.A.; Lapinte, C. Synthesis and reactivity of new heterodinuclear iron/rhenium C_x complexes of the formula (η⁵-C₅Me₅)Re(NO)(PPh₃)(C≡C)_n(η²-dppe)Fe(η⁵-C₅Me₅) (n = 3, 4): Redox properties and a dicobalt hexacarbonyl adduct. *C. R. Chim.* **2008**, *11*, 693–701. [[CrossRef](#)]
24. Meyer, W.E.; Amoroso, A.J.; Horn, C.R.; Jaeger, M.; Gladysz, J.A. Synthesis and Oxidation of Diruthenium C₄, C₆, and C₈ Complexes of the Formula (η⁵-C₅Me₅)Re(NO)(PR₃)(C≡C)_n(R₃P)(ON)Re(η⁵-C₅Me₅) (R = 4-C₆H₄R', c-C₆H₁₁): In Search of Dications and Radical Cations with Enhanced Stabilities. *Organometallics* **2001**, *20*, 1115–1127. [[CrossRef](#)]
25. Gendron, F.; Burgun, A.; Skelton, B.W.; White, A.H.; Roisnel, T.; Bruce, M.I.; Halet, J.F.; Lapinte, C.; Costuas, K. Iron and Ruthenium sigma-Polyyne of the General Formula [(M(dppe)Cp*)-(C≡C)_nR]^{0/+} (M = Fe, Ru): An Experimental and Theoretical Investigation. *Organometallics* **2012**, *31*, 6796–6811. [[CrossRef](#)]
26. Bruce, M.I.; Costuas, K.; Davin, T.; Ellis, B.G.; Halet, J.F.; Lapinte, C.; Low, P.J.; Smith, M.E.; Skelton, B.W.; Toupet, L.; et al. Iron versus ruthenium: Dramatic changes in electronic structure result from replacement of one Fe by Ru in [(Cp*)(dppe)Fe]-CC-CC-{Fe(dppe)Cp*}]ⁿ⁺ (n = 0, 1, 2). *Organometallics* **2005**, *24*, 3864–3881. [[CrossRef](#)]
27. Gückel, S.; Gluyas, J.B.G.; El-Tarhuni, S.; Sobolev, A.N.; Whiteley, M.W.; Halet, J.-F.; Lapinte, C.; Kaupp, M.; Low, P.J. Iron versus Ruthenium: Clarifying the Electronic Differences between Prototypical Mixed-Valence Organometallic Butadiynediyl Bridged Molecular Wires. *Organometallics* **2018**, *37*, 1432–1445. [[CrossRef](#)]
28. Jiao, H.J.; Costuas, K.; Gladysz, J.A.; Halet, J.F.; Guillemot, M.; Toupet, L.; Paul, F.; Lapinte, C. Bonding and electronic structure in consanguineous and conjugal iron and rhenium sp carbon chain complexes [MC₄M']ⁿ⁺: Computational analyses of the effect of the metal. *J. Am. Chem. Soc.* **2003**, *125*, 9511–9522. [[CrossRef](#)]
29. Paul, F.; Meyer, W.E.; Toupet, L.; Jiao, H.J.; Gladysz, J.A.; Lapinte, C. A “conjugal” consanguineous family of butadiynediyl-derived complexes: Synthesis and electronic ground states of neutral, radical cationic, and dicationic iron/ruthenium C₄ species. *J. Am. Chem. Soc.* **2000**, *122*, 9405–9414. [[CrossRef](#)]
30. Roberts, H.N.; Brown, N.J.; Edge, R.; Fitzgerald, E.C.; Ta, Y.T.; Collison, D.; Low, P.J.; Whiteley, M.W. Synthesis, Redox Chemistry, and Electronic Structure of the Butadiynyl and Hexatriynyl Complexes [Mo{(C≡C)_nC≡CR}(L₂)(η-C₇H₇)]^{z+} (n = 1, 2; z = 0, 1; R = SiMe₃, H; L₂ = 2,2'-bipyridine, Ph₂PCH₂CH₂PPh₂). *Organometallics* **2012**, *31*, 6322–6335. [[CrossRef](#)]
31. Brown, N.J.; Collison, D.; Edge, R.; Fitzgerald, E.C.; Low, P.J.; Helliwell, M.; Ta, Y.T.; Whiteley, M.W. Metal-stabilised diynyl radicals: Structure and reactivity of [Mo(C≡C-C≡CSiMe₃)L₂(η-C₇H₇)]^{•+} (L₂ = 2,2'-bipyridine or dppe). *Chem. Commun.* **2010**, *46*, 2253–2255. [[CrossRef](#)] [[PubMed](#)]
32. Zhuravlev, F.; Gladysz, J.A. Electronic structure and chain-length effects in diplatinum polyyne complexes trans, trans-[(X)(R₃P)₂Pt(C≡C)_nPt(PR₃)₂(X)]: A computational investigation. *Chem. Eur. J.* **2004**, *10*, 6510–6522. [[CrossRef](#)] [[PubMed](#)]
33. Bruce, M.I.; Cole, M.L.; Ellis, B.G.; Gaudio, M.; Nicholson, B.K.; Parker, C.R.; Skelton, B.W.; White, A.H. The series of carbon-chain complexes {Ru(dppe)Cp*}₂{μ-(C≡C)_x} (x = 4–8, 11): Synthesis, structures, properties and some reactions. *Polyhedron* **2015**, *86*, 43–56. [[CrossRef](#)]
34. Johnson, T.R.; Walton, D.R.M. Silylation as a Protective Method in Acetylene Chemistry—Polyyne Chain Extensions Using Reagents, Et₃Si(C≡C)_mH (m = 1, 2, 4) in Mixed Oxidative Couplings. *Tetrahedron* **1972**, *28*, 5221–5236. [[CrossRef](#)]
35. Eastmond, R.; Walton, D.R.M.; Johnson, T.R. Silylation as a Protective Method for Terminal Alkynes in Oxidative Couplings—General Synthesis of Parent Polyyne H(C≡C)_nH (n = 4–10, 12). *Tetrahedron* **1972**, *28*, 4601–4616. [[CrossRef](#)]
36. Chalifoux, W.A.; Tykwinski, R.R. Synthesis of polyyne to model the sp-carbon allotrope carbyne. *Nat. Chem.* **2010**, *2*, 967–971. [[CrossRef](#)] [[PubMed](#)]
37. Burgun, A.; Gendron, F.; Schauer, P.A.; Skelton, B.W.; Low, P.J.; Costuas, K.; Halet, J.F.; Bruce, M.I.; Lapinte, C. Straightforward Access to Tetrametallic Complexes with a Square Array by Oxidative Dimerization of Organometallic Wires. *Organometallics* **2013**, *32*, 5015–5025. [[CrossRef](#)]
38. Xia, H.P.; Jia, G.C. C₅H₅-bridged dimeric ruthenium complexes. *Organometallics* **1997**, *16*, 1–4. [[CrossRef](#)]
39. Xia, H.P.; Yeung, R.C.Y.; Jia, G.C. Synthesis of symmetrical C₅H₅-bridged dimeric ruthenium complexes. *Organometallics* **1997**, *16*, 3557–3560. [[CrossRef](#)]
40. Ribou, A.C.; Launay, J.P.; Sachtleben, M.L.; Li, H.; Spangler, C.W. Intervalence electron transfer in mixed valence diferrocenylpolyenes. Decay law of the metal-metal coupling with distance. *Inorg. Chem.* **1996**, *35*, 3735–3740. [[CrossRef](#)]
41. Liu, S.H.; Chen, Y.H.; Wan, K.L.; Wen, T.B.; Zhou, Z.Y.; Lo, M.F.; Williams, I.D.; Jia, G.C. Synthesis and characterization of linear (CH)₈-bridged bimetallic ruthenium complexes. *Organometallics* **2002**, *21*, 4984–4992. [[CrossRef](#)]

42. Liu, S.H.; Xia, H.P.; Wen, T.B.; Zhou, Z.Y.; Jia, G.C. Synthesis and characterization of bimetallic ruthenium complexes with (CH)₆ and related bridges. *Organometallics* **2003**, *22*, 737–743. [[CrossRef](#)]
43. Yuan, P.; Liu, S.H.; Xiong, W.C.; Yin, J.; Yu, G.A.; Sung, H.Y.; Williams, I.D.; Jia, G.C. Synthesis and characterization of (CH=CH)₃-bridged heterobimetallic ferrocene-ruthenium complexes. *Organometallics* **2005**, *24*, 1452–1457. [[CrossRef](#)]
44. Sahnoune, H.; Mahias, V.; Halet, J.F.; Lapinte, C. 1,4-Dimethoxybutadienediyl-Bridged Diiron Compounds in Three Oxidation States: Evaluation of Delocalization Effects. *Organometallics* **2019**, *38*, 2724–2737. [[CrossRef](#)]
45. Low, P.J. Twists and turns: Studies of the complexes and properties of bimetallic complexes featuring phenylene ethynylene and related bridging ligands. *Coord. Chem. Rev.* **2013**, *257*, 1507–1532. [[CrossRef](#)]
46. Costuas, K.; Rigaut, S. Polynuclear carbon-rich organometallic complexes: Clarification of the role of the bridging ligand in the redox properties. *Dalton Trans.* **2011**, *40*, 5643–5658. [[CrossRef](#)] [[PubMed](#)]
47. Haasler, M.; Maier, T.M.; Grotjahn, R.; Gückel, S.; Arbuznikov, A.V.; Kaupp, M. A Local Hybrid Functional with Wide Applicability and Good Balance between (De)Localization and Left–Right Correlation. *J. Chem. Theory Comput.* **2020**, *16*, 5645–5657. [[CrossRef](#)]
48. Kaupp, M.; Karton, A.; Bischoff, F.A. [Al₂O₄][−], a Benchmark Gas-Phase Class II Mixed-Valence Radical Anion for the Evaluation of Quantum-Chemical Methods. *J. Chem. Theory Comput.* **2016**, *12*, 3796–3806. [[CrossRef](#)]
49. Parthey, M.; Kaupp, M. Quantum-chemical insights into mixed-valence systems: Within and beyond the Robin-Day scheme. *Chem. Soc. Rev.* **2014**, *43*, 5067–5088. [[CrossRef](#)]
50. Renz, M.; Kess, M.; Diedenhofen, M.; Klamt, A.; Kaupp, M. Reliable Quantum Chemical Prediction of the Localized/Delocalized Character of Organic Mixed-Valence Radical Anions. From Continuum Solvent Models to Direct-COSMO-RS. *J. Chem. Theory Comput.* **2012**, *8*, 4189–4203. [[CrossRef](#)]
51. Renz, M.; Kaupp, M. Predicting the Localized/Delocalized Character of Mixed-Valence Diquinone Radical Anions. Toward the Right Answer for the Right Reason. *J. Phys. Chem. A* **2012**, *116*, 10629–10637. [[CrossRef](#)] [[PubMed](#)]
52. Ramirez-Wierzbicki, I.; Cotic, A.; Cadranet, A. Photoinduced Intervalence Charge Transfers: Spectroscopic Tools to Study Fundamental Phenomena and Applications. *ChemPhysChem* **2022**, *23*, e202200384. [[CrossRef](#)] [[PubMed](#)]
53. Pieslinger, G.E.; Ramirez-Wierzbicki, I.; Cadranet, A. The Excited-State Creutz-Taube Ion. *Angew. Chem. Int. Ed.* **2022**, *61*, e202211747. [[CrossRef](#)] [[PubMed](#)]
54. Glover, S.D.; Goeltz, J.C.; Lear, B.J.; Kubiak, C.P. Inter- or intramolecular electron transfer between triruthenium clusters: We'll cross that bridge when we come to it. *Coord. Chem. Rev.* **2010**, *254*, 331–345. [[CrossRef](#)]
55. Safari, P.; Gückel, S.; Gluyas, J.B.G.; Moggach, S.A.; Kaupp, M.; Low, P.J. The Use of Bridging Ligand Substituents to Bias the Population of Localized and Delocalized Mixed-Valence Conformers in Solution. *Chem. Eur. J.* **2022**, *28*, e202200926. [[CrossRef](#)] [[PubMed](#)]
56. Harrison, D.P.; Grotjahn, R.; Naher, M.; Ghazvini, S.; Mazzucato, D.M.; Korb, M.; Moggach, S.A.; Lambert, C.; Kaupp, M.; Low, P.J. Quantum Interference in Mixed-Valence Complexes: Tuning Electronic Coupling Through Substituent Effects. *Angew. Chem. Int. Ed.* **2022**, *61*, e202211000. [[CrossRef](#)] [[PubMed](#)]
57. Bartlett, M.J.; Frogley, B.J.; Hill, A.F.; Sharma, M.; Smith, M.K.; Ward, J.S. Hydrogenating an organometallic carbon chain: Buten-yn-diyl (CH=CHC≡C) as a missing link. *Dalton Trans.* **2019**, *48*, 16534–16554. [[CrossRef](#)]
58. Wuttke, E.; Pevny, F.; Hervault, Y.M.; Norel, L.; Drescher, M.; Winter, R.F.; Rigaut, S. Fully Delocalized (Ethyne)(vinyl)phenylene Bridged Triruthenium Complexes in up to Five Different Oxidation States. *Inorg. Chem.* **2012**, *51*, 1902–1915. [[CrossRef](#)]
59. Olivier, C.; Costuas, K.; Choua, S.; Maurel, V.; Turek, P.; Saillard, J.Y.; Touchard, D.; Rigaut, S. “Chain-Like” Trimetallic Ruthenium Complexes with C₇ Carbon-Rich Bridges: Experimental and Theoretical Investigations of Electronic Communication Tuning in Five Distinct Oxidation States. *J. Am. Chem. Soc.* **2010**, *132*, 5638–5651. [[CrossRef](#)]
60. Vacher, A.; Benameur, A.; Ndiaye, C.M.; Touchard, D.; Rigaut, S. Linked C-7 Carbon-Rich Bridges: A New Dimension for Ruthenium Redox-Active Organometallics. *Organometallics* **2009**, *28*, 6096–6100. [[CrossRef](#)]
61. Rigaut, S.; Olivier, C.; Costuas, K.; Choua, S.; Fadhel, O.; Massue, J.; Turek, P.; Saillard, J.Y.; Dixneuf, P.H.; Touchard, D. C₇ and C₉ carbon-rich bridges in diruthenium systems: Synthesis, spectroscopic, and theoretical investigations of different oxidation states. *J. Am. Chem. Soc.* **2006**, *128*, 5859–5876. [[CrossRef](#)] [[PubMed](#)]
62. Rigaut, S.; Perruchon, J.; Guesmi, S.; Fave, C.; Touchard, D.; Dixneuf, P.H. Carbon-rich ruthenium complexes containing Bis(allynylidene) and mixed alkynyl-allynylidene bridges. *Eur. J. Inorg. Chem.* **2005**, *2005*, 447–460. [[CrossRef](#)]
63. Hall, M.R.; Korb, M.; Moggach, S.A.; Low, P.J. Further Chemistry of Ruthenium Alkenyl Acetylide Complexes: Routes to Allynylidene Complexes via a Series of Electrophilic Addition Reactions. *Organometallics* **2020**, *39*, 2838–2853. [[CrossRef](#)]
64. Hall, M.R.; Korb, M.; Moggach, S.A.; Low, P.J. Oxidative Coupling of Ruthenium Alkenyl Acetylide Complexes as a Route to Dinuclear Complexes Featuring Carbon-Rich Bridging Ligands. *Organometallics* **2022**, *41*, 2958–2973. [[CrossRef](#)]
65. Li, Y.; Blacque, O.; Fox, T.; Luber, S.; Polit, W.; Winter, R.F.; Venkatesan, K.; Berke, H. Electronic communication in phosphine substituted bridged diruthenium complexes—Clarifying ambiguities raised by the redox non-innocence of the C₄H₂- and C₄-bridges. *Dalton Trans.* **2016**, *45*, 5783–5799. [[CrossRef](#)] [[PubMed](#)]
66. Bruce, M.I.; Ellis, B.G.; Low, P.J.; Skelton, B.W.; White, A.H. Syntheses, structures, and spectro-electrochemistry of {Cp*(PP)Ru}C≡CC≡C{Ru(PP)Cp*} (PP = dppm, dppe) and their mono- and dications. *Organometallics* **2003**, *22*, 3184–3198. [[CrossRef](#)]
67. Hall, M.R.; Moggach, S.A.; Low, P.J. Syntheses and Structures of trans-bis(Alkenylacetylide) Ruthenium Complexes. *Chem. Asian, J.* **2021**, *16*, 3385–3403. [[CrossRef](#)]

68. Kaupp, M.; Renz, M.; Parthey, M.; Stolte, M.; Wurthner, F.; Lambert, C. Computational and spectroscopic studies of organic mixed-valence compounds: Where is the charge? *Phys. Chem. Chem. Phys.* **2011**, *13*, 16973–16986. [[CrossRef](#)]
69. Ladjarafi, A.; Costuas, K.; Meghezzi, H.; Halet, J.F. Electronic structure of modeled vs. real carbon-chain containing organometallic dinuclear complexes: Similarities and differences. *J. Mol. Model.* **2015**, *21*, 71. [[CrossRef](#)]
70. Scott, A.P.; Radom, L. Harmonic vibrational frequencies: An evaluation of Hartree-Fock, Moller-Plesset, quadratic configuration interaction, density functional theory, and semiempirical scale factors. *J. Phys. Chem.* **1996**, *100*, 16502–16513. [[CrossRef](#)]
71. Bruce, M.I.; Costuas, K.; Ellis, B.G.; Halet, J.F.; Low, P.J.; Moubaraki, B.; Murray, K.S.; Ouddai, N.; Perkins, G.J.; Skelton, B.W.; et al. Redox-active complexes containing group 8 metal centers linked by C₂ bridges. *Organometallics* **2007**, *26*, 3735–3745. [[CrossRef](#)]
72. Bruce, M.I.; Low, P.J.; Costuas, K.; Halet, J.F.; Best, S.P.; Heath, G.A. Oxidation chemistry of metal-bonded C₄ chains: A combined chemical, spectroelectrochemical, and computational study. *J. Am. Chem. Soc.* **2000**, *122*, 1949–1962. [[CrossRef](#)]
73. Parthey, M.; Gluyas, J.B.G.; Schauer, P.A.; Yufit, D.S.; Howard, J.A.K.; Kaupp, M.; Low, P.J. Refining the Interpretation of Near-Infrared Band Shapes in a Polyynediyl Molecular Wire. *Chem. Eur. J.* **2013**, *19*, 9780–9784. [[CrossRef](#)] [[PubMed](#)]
74. Bruce, M.I.; Hall, B.C.; Low, P.J.; Smith, M.E.; Skelton, B.W.; White, A.H. Heterometallic complexes containing C₄ chains. X-ray structures of {Cp(OC)₃W}C≡CC≡C{Ir(CO)(PPh₃)₂(O₂)} and *cis*-Pt{C≡C[W(CO)₃Cp]}₂(PEt₃)₂. *Inorg Chim Acta* **2000**, *300*, 633–644. [[CrossRef](#)]
75. Brady, M.; Weng, W.Q.; Zhou, Y.L.; Seyler, J.W.; Amoroso, A.J.; Arif, A.M.; Bohme, M.; Frenking, G.; Gladysz, J.A. Consanguineous families of coordinated carbon: A ReC₄Re assembly that is isolable in three oxidation states, including crystallographically characterized ReC≡CC≡CRe and Re⁺=C=C=C=C=Re⁺ adducts and a radical cation in which charge is delocalized between rhenium termini. *J. Am. Chem. Soc.* **1997**, *119*, 775–788.
76. Weng, W.G.; Bartik, T.; Gladysz, J.A. Towards One-Dimensional Carbon Wires Connecting Single Metal Centers—A Cumulenyl C₅ Chain That Mediates Charge-Transfer between Rhenium and Manganese Termini. *Angew. Chem. Int. Ed.* **1994**, *33*, 2199–2202. [[CrossRef](#)]
77. Seyler, J.W.; Weng, W.Q.; Zhou, Y.L.; Gladysz, J.A. An Isolable Organometallic Cation-Radical in Which a C₄ Chain Conducts Charge between 2 Chiral and Configurational Stable Rhenium Termini. *Organometallics* **1993**, *12*, 3802–3804. [[CrossRef](#)]
78. Lear, B.J.; Chisholm, M.H. Oxalate Bridged MM (MM = Mo₂, MoW, and W₂) Quadruply Bonded Complexes as Test Beds for Current Mixed Valence Theory: Looking beyond the Intervalence Charge Transfer Transition. *Inorg. Chem.* **2009**, *48*, 10954–10971. [[CrossRef](#)]
79. Szeghalmi, A.V.; Erdmann, M.; Engel, V.; Schmitt, M.; Amthor, S.; Kriegisch, V.; Noll, G.; Stahl, R.; Lambert, C.; Leusser, D.; et al. How delocalized is N,N,N',N'-tetraphenylphanylenediamine radical cation? An experimental and theoretical study on the electronic and molecular structure. *J. Am. Chem. Soc.* **2004**, *126*, 7834–7845. [[CrossRef](#)]
80. Badger, B.; Brocklehurst, B. Absorption spectra of dimer cations. Part 4—Theoretical considerations and dimer structure. *Trans. Faraday Soc.* **1970**, *66*, 2939–2947. [[CrossRef](#)]
81. Connelly, N.G.; Geiger, W.E. Chemical redox agents for organometallic chemistry. *Chem. Rev.* **1996**, *96*, 877–910. [[CrossRef](#)] [[PubMed](#)]
82. Sheldrick, G.M. SHELXT—Integrated space-group and crystal-structure determination. *Acta Crystallogr. A* **2015**, *71*, 3–8. [[CrossRef](#)] [[PubMed](#)]
83. Sheldrick, G.M. Crystal structure refinement with SHELXL. *Acta Crystallogr. C* **2015**, *71*, 3–8. [[CrossRef](#)] [[PubMed](#)]
84. Dolomanov, O.V.; Bourhis, L.J.; Gildea, R.J.; Howard, J.A.K.; Puschmann, H. OLEX2: A complete structure solution, refinement and analysis program. *J. Appl. Crystallogr.* **2009**, *42*, 339–341. [[CrossRef](#)]
85. Puschmann, H.; Dolomanov, O. Olex(2): A Comprehensive Molecular Graphics Tool for Small-Molecule Structures. *Acta Crystallogr. A* **2006**, *62*, S246. [[CrossRef](#)]
86. Farrugia, L.J. WinGX and ORTEP for Windows: An update. *J. Appl. Crystallogr.* **2012**, *45*, 849–854. [[CrossRef](#)]
87. Frisch, M.J.; Trucks, G.W.; Schlegel, H.B.; Scuseria, G.E.; Robb, M.A.; Cheeseman, J.R.; Scalmani, G.; Barone, V.; Petersson, G.A.; Nakatsuji, H.; et al. *Gaussian 09, Revision, A.02*; Gaussian, Inc.: Wallingford, CT, USA, 2016.
88. O'Boyle, N.M.; Tenderholt, A.L.; Langner, K.M. cclib: A library for package-independent computational chemistry algorithms. *J. Comput. Chem.* **2008**, *29*, 839–845. [[CrossRef](#)]
89. Wadt, W.R.; Hay, P.J. Abinitio Effective Core Potentials for Molecular Calculations—Potentials for Main Group Elements Na to Bi. *J. Chem. Phys.* **1985**, *82*, 284–298. [[CrossRef](#)]
90. Hay, P.J.; Wadt, W.R. Abinitio Effective Core Potentials for Molecular Calculations—Potentials for K to Au Including the Outermost Core Orbitals. *J. Chem. Phys.* **1985**, *82*, 299–310. [[CrossRef](#)]
91. Hay, P.J.; Wadt, W.R. Abinitio Effective Core Potentials for Molecular Calculations—Potentials for the Transition-Metal Atoms Sc to Hg. *J. Chem. Phys.* **1985**, *82*, 270–283. [[CrossRef](#)]
92. Petersson, G.A.; Allaham, M.A. A Complete Basis Set Model Chemistry. 2. Open-Shell Systems and the Total Energies of the 1st-Row Atoms. *J. Chem. Phys.* **1991**, *94*, 6081–6090. [[CrossRef](#)]
93. Petersson, G.A.; Bennett, A.; Tensfeldt, T.G.; Allaham, M.A.; Shirley, W.A.; Mantzaris, J. A Complete Basis Set Model Chemistry.1. The Total Energies of Closed-Shell Atoms and Hydrides of the 1st-Row Elements. *J. Chem. Phys.* **1988**, *89*, 2193–2218. [[CrossRef](#)]
94. Klamt, A. The COSMO and COSMO-RS solvation models. *Wires Comput. Mol. Sci.* **2011**, *1*, 699–709. [[CrossRef](#)]
95. Klamt, A. Calculation of UV/Vis spectra in solution. *J. Phys. Chem.* **1996**, *100*, 3349–3353. [[CrossRef](#)]

-
96. Martin, R.L. Natural transition orbitals. *J. Chem. Phys.* **2003**, *118*, 4775–4777. [[CrossRef](#)]
 97. Krejcik, M.; Danek, M.; Hartl, F. Simple Construction of an Infrared Optically Transparent Thin-Layer Electrochemical-Cell—Applications to the Redox Reactions of Ferrocene, $\text{Mn}_2(\text{CO})_{10}$ and $\text{Mn}(\text{CO})_3(3,5\text{-Di-Tert-Butyl-Catecholate})^-$. *J. Electroanal. Chem.* **1991**, *317*, 179–187. [[CrossRef](#)]

Disclaimer/Publisher’s Note: The statements, opinions and data contained in all publications are solely those of the individual author(s) and contributor(s) and not of MDPI and/or the editor(s). MDPI and/or the editor(s) disclaim responsibility for any injury to people or property resulting from any ideas, methods, instructions or products referred to in the content.